Recommended Practice for Use of ExB Probes in Electric Propulsion Testing

IEPC-2025-483

Presented at the 39th International Electric Propulsion Conference Imperial College • London, United Kingdom September 14-19, 2025

Joshua L. Rovey.¹ and Toyofumi Yamauchi.² University of Illinois Urbana-Champaign, Urbana, Illinois, 61801, USA

Wensheng Huang³ and Robert E. Thomas.⁴ *NASA Glenn Research Center, Cleveland, Ohio, 44135, USA*

William J. Hurley.⁵
University of Michigan, Ann Arbor, Michigan, 48109, USA

Shawn C. Farnell⁶, Seth J. Thompson⁷, Cody C. Farnell⁸, and Casey C. Farnell⁹ *Colorado State University / Plasma Controls LLC, Fort Collins, Colorado, 80523, USA*

William P. Brabston¹⁰ Georgia Institute of Technology, Atlanta, Georgia, 30318, USA

and

Jason A. Young. ¹¹
Aerospace Corporation, California, USA

An ExB probe is an electric propulsion plume diagnostic that has at its core a Wien filter. Ions entering the instrument experience perpendicular electric and magnetic fields, and opposing electric and magnetic forces, and are filtered based on their velocity. While the ExB probe can be used to estimate ion velocity distribution function, in the electric propulsion community, it is commonly used to measure plume current and species fractions. There are numerous probe designs, implementation and operation procedures, and data analysis approaches described and in use across the community. This paper provides recommendations and descriptions of best practices for design, implementation, and data analysis for the ExB probe, with a

¹ Professor, Aerospace Engineering, <u>rovey@illinois.edu</u>

² PhD Candidate, Aerospace Engineering, <u>ty20@illinois.edu</u>

³ Research Engineer, Electric Propulsion Systems Branch, wensheng.huang@nasa.gov

⁴ Research Engineer, Electric Propulsion Systems Branch, <u>robert.e.thomas@nasa.gov</u>

⁵ PhD Candidate, Aerospace Engineering, <u>wjhurley@umich.edu</u>

⁶ Research Scientist II / Research Scientist, Mechanical Engineering, shawn.farnell@plasmacontrols.com

⁷ Research Scientist II / Research Scientist, Mechanical Engineering, seth.thompson@colostate.edu

⁸ Research Scientist II / Chief Scientist, Mechanical Engineering, cody.farnell@plasmacontrols.com

⁹ Research Scientist II / President, Mechanical Engineering, casey.farnell@plasmacontrols.com

¹⁰ PhD Candidate, Aerospace Engineering, wbrabston3@gatech.edu

¹¹ Research Scientist, <u>jason.a.young@aero.org</u>

particular emphasis on Hall and Ion thrusters. This work contributes to the broader community goal to standardize the use of diagnostics in electric propulsion testing.

Nomenclature

		Nomenciature
$A_{beam,k}$	=	Ion beam cross-section area, m ²
a, b, c, d, n, 6) =	Model and distribution function fitting parameters
B , \vec{B}	=	Applied magnetic field, T
B_{eff}	=	Effective magnetic field, T
B_o	=	Magnetic field at mid-point of the filter, T
B_{pra}	=	Practical magnetic field, T
d, d_e	=	Electrode plate separation distance, m
E, \vec{E}	=	Applied electric field, V/m
E_{eff}	=	Effective electric field, V/m
E_o	=	Electric field at mid-point of the filter, V/m
e	=	Elementary charge of an electron,
$ec{F}$	=	Force, N
f_k	=	Ion velocity distribution function, -
G	=	Probe geometric constant, m ⁻¹
g_k	=	Measured probe spectra, -
I	=	Identity matrix
I_j, I_k	=	Measured probe current, A
l_c	=	Collimator length, m
l_d	=	Drift tube length, m
l_f	=	Wien filter length, m
J	=	Current density, A/m ²
j, k	=	Species, -
m	=	Mass of a charged particle, kg
n_k	=	Ion number density, m ⁻³
n_o	=	Background neutral number density, m ⁻³
q, q_k	=	Charge, C
R	=	Voltage divider resistance, Ω
$r_{i=1,2,3,4}$	=	Aperture radius for different components along the beam line, m
T_k	=	Transmittancy matrix, -
V_{accel}	=	Ion accelerating potential difference, V
V_p	_	Plasma potential, V
V_{plates}		Electric potential difference across probe electrodes, V
$V_{plates,range}$	=	Recommended range of V_{plates} values, V
v, \vec{v}, v_{ion}	=	Ion velocity, m/s
v_{Wien}, v_{W}	=	Wien velocity, m/s
$v_{w,eff}$		Effective Wien velocity, m/s
Z,Z_j	=	Charge state, -
Z	=	Axial position downstream of thruster, m
α_{max}	=	Maximum collimator acceptance angle, radian Secondary electron emission yield, -
$oldsymbol{\gamma}_k$	=	Error or noise
ζ_j	=	Species fraction of the j-th species, -
λ	=	Regularization parameter, -
σ_i	=	Charge-exchange cross-section, m ⁻³
$\Omega_{m{i}}$	=	Current fraction of the j-th species, -
32j	_	current fraction of the j-th species, -

I. Introduction

A major challenge across the space electric propulsion (EP) community is the standardization of practices, techniques, and approaches for the measurement and testing of EP devices. There is a need for accurate, consistent, repeatable test results and the ability to compare results from different test facilities operated by different organizations, groups, and researchers. This can only be achieved through the development and application of common procedures and standards of measurement practice. If EP devices and technology are to continue to proliferate and transition from laboratory to flight, then there is a corresponding need for community standards.

With these challenges in mind, a previous effort by the American Institute of Aeronautics and Astronautics (AIAA) Electric Propulsion Technical Committee led to the publication of a series of papers on recommended practices for some of the important diagnostic and measurement approaches used in EP testing. Specifically, recommended practices were developed for pressure measurement and pumping speed calculations [1], flow control and measurement [2], thrust measurements [3], and use of the Faraday probe [4], Langmuir probe [5], emissive probe [6], inductive magnetic field probe [7], and electrostatic analyzer [8] in determining electromagnetic, plasma, and ion beam properties. While these have greatly aided the community, there are still additional diagnostics and techniques that lack recommendations and standardization of their application to EP testing. One of these additional diagnostics is the ExB ("E cross B") probe, which is the subject and focus of this paper.

An ExB probe is a composite instrument that has a Wien filter at its core. It is a band-pass ion velocity filter that uses electric and magnetic fields that are orthogonal to each other and the ion velocity. This triad selectively filters ions based on their velocity. While the ExB probe can provide a measure of the ion velocity distribution function (IVDF), in the EP community, it is often configured as a mass spectrometer (or separator) and used to measure the ratios of the different charged species present in the emitted ion plume of a thruster. For example, when operating with a single noble gas propellant, e.g., xenon, as is common in EP testing, the ExB probe is used to measure the ratios of multiply charged ions in the plume. Multiply-charged ions reduce thruster efficiency [9], deposit more energy into thruster walls [10], and cause higher ion bombardment sputter erosion [11,12], so accurate characterization of multiply-charged species content is important for understanding and predicting thruster performance, lifetime, and spacecraft integration.

This paper describes recommended practices for ExB probe design, operation, and data analysis in electric propulsion testing. The following sections provide a brief history of the invention, development, and application of the probe to EP testing, and an overview of probe theory. Specific examples of ExB probes and their dimensions are provided in the design section, and recommendations on the implementation and operation of the probe are described. Probe data analysis for both estimating the IVDF and determining plume species current and charge-state fractions is described. Finally, a comparison is provided of the ExB probe with other common EP plume diagnostics for measuring similar properties. Recommended practices are contained throughout the manuscript.

II. A Brief History

A charged-particle velocity filter with orthogonal electric and magnetic fields was first documented by Wilhelm Wien in 1897 [13-16]. Wien used it to make one of the first measurements of the charge-to-mass ratio of electrons, and thereby showed that the cathode ray consists of particles with mass. Over the next fifty years, variants of the Wien filter (although it was rarely called that) were used extensively within the particle physics community. A typical implementation might include features such as electric and magnetic fields in tandem rather than superimposed and curved or even circular geometries rather than the straight geometries used for EP diagnostics.. In many cases the instrument was used to study the effect of electric and magnetic fields on beam focusing and dispersion [15,16]. The Wien filter has been and is still used in a variety of electron optics systems [17]. It has been used as an electron monochromator since the 1960s [18] -- the use of two Wien filters as a double focus electron monochromator is still common today [19]. Further, the Wien filter is used to separate primary and secondary electrons [20], compensate for dispersion, second-order and higher-order aperture aberrations [21,22], and correct for chromatic and spherical aberrations in electron optics [22-24].

Perhaps one of the first descriptions of a Wien filter as a mass spectrometer (spectrograph) for heavy ions was by Bainbridge in 1933 [25]. Bainbridge describes an instrument with superimposed electric and magnetic fields and a set of beam collimating apertures for studying heavy ion isotopes. Seliger was perhaps the first to use the term ExB when referring to the instrument as an ExB mass separator in 1972 [26]. Seliger developed, linearized, and solved the governing equations for ion trajectories in an ExB mass separator and was focused primarily on beam astigmatism in isotope separation and ion implantation. Holmlid expanded upon this work in 1975 focusing on the mass dispersion and resolution of the Wien filter with homogeneous, purely orthogonal, electric and magnetic fields [27]. Since that time, the Wien filter has been used as an ExB mass spectrometer for a myriad of applications [28-32]. However, the

EP community appears to be unique in its focus on using the Wien filter to measure and quantify multiply charged species in ion beams and plumes.

The Wien filter spectrometer was used in electric propulsion testing for the first time in 1973 by Vahrenkamp [33]. Vahrenkamp employed the probe to measure the singly, doubly, and triply charged mercury ion populations in the plume of a gridded ion thruster and incorporated these measurements into performance calculations. A subsequent parametric investigation developed correlations between the multiply-charged ion population and mass utilization efficiency [34]. Since that time the ExB probe has been used extensively to diagnose ion thruster performance and operation. Sovey used an ExB probe to show that, compared to a divergent magnetic field configuration, a ring-cusp magnetic field configuration in the discharge chamber has less centerline screen grid erosion due to lower concentration of doubly-charged ions for argon, krypton, and xenon propellants [35]. Williams et al. showed that the ratio of doubly-to-singly charged plume ions can be directly related to measured and calculated erosion rates of the grids of 30 and 40 cm xenon ion thrusters [36]. Pollard et al. used spatially-resolved charge-state distributions to derive thrust correction factors for a 36-cm NEXT ion thruster [37]. The ExB probe has become a common and important diagnostic in ion thruster wear tests [38], long-duration tests [40], and integration tests [41].

The Wien filter was first employed to study Hall thrusters by Kim and Gallimore, and they used it to investigate the plume of the SPT-100 [42,43]. Hofer and Gallimore used an ExB probe to interrogate the multiply-charged species content of the NASA-173Mv2 xenon ion plume [44], measuring doubly-charged fractions of 4-12% and triply-charged ion fractions of 1-2%, and then used these measurements in an efficiency analysis [45]. Ekholm and Hargus measured multiply-charged species in the plume of a 200 W xenon Hall thruster [46]. Reid et al. explored the angular dependence of multiply-charged species fractions [47]. Sullivan et al. used the ExB as a collimated velocity filter to map out the origins and trajectories of primary ions emanating from a Hall thruster [48]. Diamant et al. have used ExB probe measurements to characterize background pressure effects on Hall thrusters [49], as well as the performance and plume properties of 2 kW [50] and 1.5 kW [51] Hall thrusters. More recently, Gurciullo et al. have used an ExB probe to investigate the ion plume of a Hall thruster operating with xenon-nitrogen and xenon-air mixtures [52], and Watanabe et al. explored the performance and plume of an 85 W class Hall thruster [53]. Hall et al. used an ExB probe to characterize the plume of a 100 kW nested channel Hall thruster [54]. Similar to ion thrusters, the ExB probe has become commonplace in Hall thruster wear testing and long duration testing [55,56].

III. Theory

An ExB probe is a composite instrument that consists of multiple sections along the beam line, including at least an entrance aperture, Wien filter, and collector to record ions. In addition, an entrance collimator, drift section, and suppressor aperture are also commonly included, as shown in Figure 1. Ions enter the probe from the outside plasma plume through the entrance aperture. Two apertures can be used to set a probe centerline axis and allow for a general ion acceptance angle into the probe. Some ions entering the probe traverse each section and reach the collector and register a current, while others are unable to reach the collector. For example, ions off centerline are physically stopped at the collimator or at the entrance to the Wien filter. Ions that enter the Wien filter experience electric and magnetic forces. If the electric and magnetic forces are balanced and there is no net force on the ion, then it passes through the filter (red arrow going through the filter in Figure 1). If there is a net force on the ion then it is pushed off axis, resulting in ions that strike the filter electrodes, drift tube surfaces, or suppressor aperture structure. Specifically, as shown in Figure 1, if the magnetic force dominates then the ion trajectory bends down (negative-y direction), and if the electric force dominates then it bends up (positive-y direction). Finally, ions that do reach the collector can cause secondary electron creation and emission from that surface. An electron suppressor structure can be used and electrically biased negative of the collector to return secondary electrons to the collector.

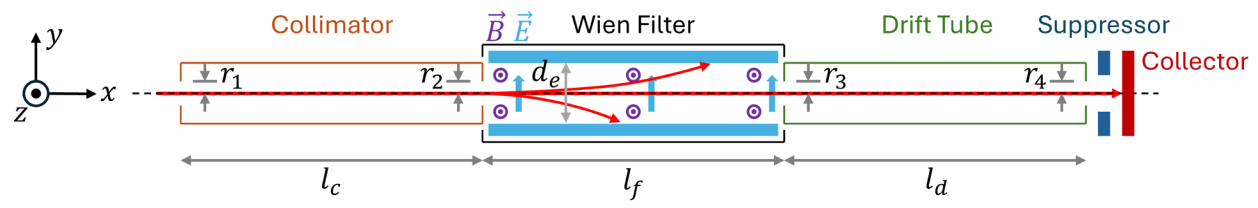


Figure 1: ExB probe schematic.

A. First Principles

Comprehensive modeling of charged particle motion through the instrument includes the entire composite ExB probe structure, but here the initial analysis focuses on only the Wien filter. In the Wien filter, ions experience

superimposed electric and magnetic forces. Charged particle motion in electric and magnetic fields is governed by the Lorentz force equation, Eq. 1, where q is the particle charge, \vec{E} is the electric field, \vec{v} is the ion velocity, and \vec{B} is the magnetic field. Particles that pass through the filter experience no net force. In this situation, Eq. 2 shows that the electric field can be written in terms of the charged particle velocity and magnetic field. As shown in Figure 1, the triad of particle velocity, electric field, and magnetic field are typically set up to be an orthogonal system. For the purposes of this paper, ion velocity, electric field, and magnetic field are assumed to be in the x, y, and z directions, respectively. Equation 3 shows that the particle velocity passing through the filter (Wien velocity) can be selected by changing the magnitude of the electric and/or magnetic field. Ions with velocity slower than the Wien velocity experience a net force in the electric field direction, while ions with faster velocity experience a net force opposite to the electric field direction.

$$\vec{F} = q(\vec{E} + \vec{v} \times \vec{B}) = 0$$

$$\vec{E} = -\vec{v} \times \vec{B}$$
 2

$$v = -\frac{E}{R} = v_{Wien}$$
 3

Typically, a constant magnetic field is applied with permanent magnets and the electric field is created by applying a known electric potential difference between two parallel plates, V_{plates} , separated by a gap distance, d, as shown in Eq. 4. Combining Eqs. 3 and 4 into Eq. 5 shows that the ion velocity selected to pass through the filter can be adjusted by changing V_{plates}. In this way, the Wien filter acts as a charged particle velocity filter.

$$E = \frac{V_{plates}}{d}$$

$$E = \frac{V_{plates}}{d}$$

$$v = v_{Wien} = -\frac{V_{plates}}{Bd}$$
5

The Wien filter is also used as a particle mass analyzer or mass spectrometer, or more specifically, as a particle charge-to-mass ratio analyzer. Conservation of energy requires that the change in kinetic energy of an ion with charge, q, and mass, m, is related to the change in electric potential energy, V_{accel} , as shown in Eq. 6 (assuming the ion starts from rest).

$$v = \sqrt{\frac{2qV_{accel}}{m}}$$

If all ions are accelerated by the same change in electric potential, V_{accel} , then the ion charge-to-mass ratio can be expressed as a function of the ExB probe plate potential difference, V_{plates}, by combining Eqs. 5 and 6 into Eq. 7. The Wien filter is a particle charge-to-mass ratio filter.

$$\frac{q}{m} = \frac{1}{2V_{accel}} \left(\frac{V_{plates}}{Bd}\right)^2$$
 7

Finally, in the case where all particles have the same mass, m, and the particle charge, q, is expressed as a multiple, Z, of the fundamental charge, e(q = Ze), then the Wien filter can be used as a particle charge-state filter, Eq. 8. Note that in ExB data (spectra) the peaks associated with different charge states are separated by the square-root of the plate potential difference. This is the common application in Hall-effect thruster and gridded ion thruster tests to measure the multiply-charge ion composition of the plume, e.g., the fraction of plume ion species that are singly-, doubly-, triply-charged xenon.

$$Z = \frac{m}{2eV_{accel}} \left(\frac{V_{plates}}{Bd}\right)^2$$
 8

B. Non-uniform fields

In a real Wien filter, one must account for the fact that the electric and magnet fields are not perfectly uniform. For the B-field, the best practice is to measure the actual field along the probe centerline. Instead of measuring only the peak B-field strength and assuming the peak value is constant and uniform along the axis, it is recommended to measure the entire B-field axial distribution, ideally by using a motion stage to translate a magnetic field probe attached to a Gaussmeter. If comprehensive direct measurements are not feasible, the next best approach is to simulate the field profile using the probe geometry and a 3D finite-element EM field simulator, such as Ansys Maxwell or COMSOL AC/DC Module. While simulated field shapes are generally reliable, the absolute field strength often deviates from actual values, so at least one direct measurement datapoint is needed for scaling. Due to the challenges in measuring the E-field, a 3D EM field simulation is typically the best option. Although a 2D finite-element EM simulator, such as FEMM, offers faster simulations and is often available for free, it should be used only for early-stage design, as it lacks the full accuracy needed for final analysis. Effective electric (E_{eff}) and magnetic field strengths (B_{eff}) can be calculated from the measured or simulated field profiles (E(x)) and B(x) using Eqs. 9 and 10, respectively. The effective Wien velocity that accounts for the field non-uniformity is given by Eq. 11 [57]. In this equation, B_{pra} is the practical B-field strength, and E_0 is the E-field strength at the center of the filter section, which typically matches well with V_{plates}/d_e . The ratio of the effective to the center E-field strength (E_{eff}/E_0) is generally close to, but less than, one, and independent of the applied potential difference (V_{plates}).

$$E_{eff} = \frac{1}{l_f} \int_0^{l_f} E(x) dx$$
 9

$$B_{eff} = \frac{1}{l_f} \int_0^{l_f} B(x) dx$$
 10

$$v_{w,eff} = \frac{E_{eff}}{B_{eff}} = \frac{V_{plates}}{d_e} \frac{1}{B_{pra}} = \frac{V_{plates}}{d_e} \frac{E_{eff}/E_0}{B_{eff}}$$

Figure 2 shows the simulated E- and B-fields for the typical ExB probe geometries. The x-axis corresponds to the axial distance from the center of the filter section normalized to the filter section length l_f . The E- and B-fields are normalized to their values at z=0 ($E_{y,0}$ and $B_{z,0}$): 9999.7 V/m and 0.144 Tesla, respectively. The effective E- and B-field strengths are 9743.9 V/m (~97.4% of $E_{y,0}$) and 0.126 Tesla (~87.5% of $B_{z,0}$), respectively. The practical B-field strength is 0.129 Tesla, which is ~89.5% of the B-field strength at the center of the filter section. This difference can cause systematic error in the calculated ion velocity.

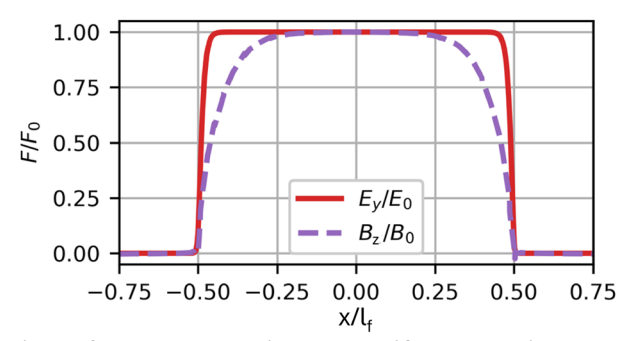


Figure 2: Example typical non-uniform electric and magnetic field profiles along the ExB probe axis (x-axis in Figure 1).

C. Instrument Velocity Resolution

The Wien filter analyzed in the previous section is only one part of the composite ExB instrument (as shown in Figure 1), and more complex models account for the transmission of ions through all parts of the probe. In other words, real-world effects such as the finite geometry and size of the instrument, non-uniformity of the applied fields, particle collisions, and non-axial velocity component enable ions that are not at the ExB Wien velocity to pass through the probe and be collected. Huang and Shastry consider the effects of finite probe geometry and size by linearizing the equation of particle motion through the probe and assuming a small acceptance angle of charged particles [58].

The resulting probe velocity resolution, which is the range of particle velocities transmitted through the probe, Δv , is shown in Eq. 12, where G is a constant based on the probe geometry and size, i.e., collimator length, aperture radii, filter length, etc., and is described in Huang and Shastry [58]. Equation 13 is the velocity resolution in terms of relative percentage of the Wien velocity. The probe resolution in relative percentage increases with the velocity of the particle.

$$\Delta v = \frac{mv_{Wien}^2}{Z_{eB}}G$$

$$\Delta v = \frac{mv_{Wien}^2}{ZeB}G$$

$$\frac{\Delta v}{v_{Wien}} = \frac{mv_{Wien}}{ZeB}G$$
12

From Eqs. 12 and 13 it is clear that the velocity resolution is broader (worse) for larger Wien velocity, larger ion mass, and smaller ion charge state. These trends are illustrated in Figure 3 for xenon ions and two different conceptual ExB probe designs (A and B). Probes A and B have design such that G in Eqs. 12 and 13 is 0.208 and 0.364 m⁻¹, respectively, and the magnetic field is assumed to be 0.2 T in both probes. The assumed probe dimensions are given in Table 1 and correspond to Figure 1. Generally, probe A is a longer Wien filter length and/or smaller orifices, which yields a smaller geometric constant, G, and narrower velocity resolution. Figure 3 shows plots of the velocity of ions entering the probe that are collected (y-axis) as a function of the imposed Wien velocity (x-axis). In the ideal case, the only ion velocity passing through the probe would be exactly the Wien velocity (Eq. 5). In reality, a range of ion velocity is collected. Each plot in Figure 3 shows two white dashed curves that are the maximum and minimum ion velocity collected by the probe at a given Wien velocity due to finite resolution (Eq. 12).

Table 1: Example ExB probe design dimensions.

			Rac (m		S	Length (mm)			Plate Sep. (mm)	Magnetic Field (T)	(1/m)
P	robe	r1	r2	r3	r4	lc	1f	ld	de	В	G
	A	1	2	3	4	100	200	50	10	0.2	0.208
	В	1	2	3	4	100	125	50	10	0.2	0.364

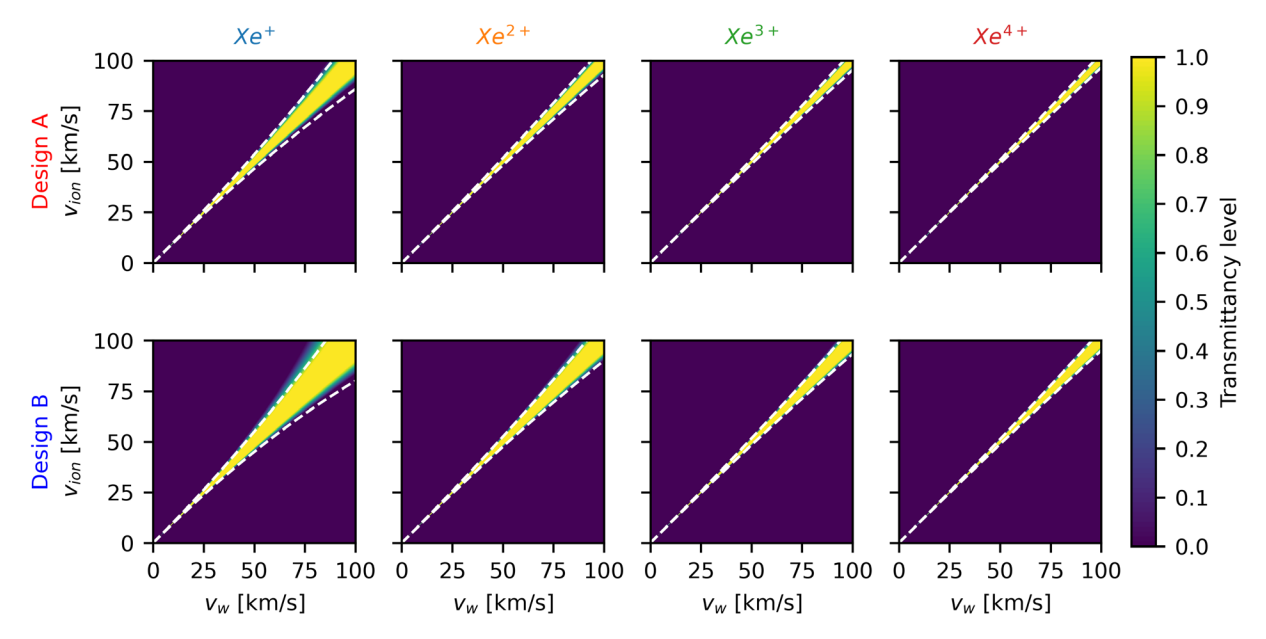


Figure 3: Resolution and transmittancy of two different ExB probe designs of Table 1.

Figure 4 shows the effect of probe velocity resolution on the resulting measured ExB probe spectra for xenon ion beams. Figure 4A shows a notional narrow beam energy distribution representative of a gridded ion thruster (GIT), while Figure 4B shows a broader energy beam representative of a Hall-effect thruster (HET). Both are shown with up to quadruply-charged ions. The measured ExB probe spectra are different depending on the probe geometry and corresponding probe velocity resolution. For a narrow beam energy source like a GIT, even the wide velocity resolution probe B measures a spectrum with clear separation between the different ion charge-state species. The velocity resolution is so wide that it collects the entirety of each different charged species and the spectrum is a series of approximately flat constant current measurements for each species. While the shape of the measured ExB spectrum is different than the true IVDF, it is relatively straightforward to compare the magnitude of each plateau and thereby estimate the relative species fractions. For a broader beam source like the HET, the IVDFs of the different charge-state species overlap. In this case, the wide velocity resolution of probe B is unacceptable. Even the narrower resolution probe A measures a spectrum with overlap and convolution of the IVDFs of the different species. In general, a recommended rule of thumb is that the probe velocity resolution should be an order of magnitude smaller than the width of the IVDF so that the IVDF can be resolved. However, this is not always possible because a confounding tradeoff is that narrower velocity resolution generally results in lower signal-to-noise ratio. This effect can also be observed in Figure 4B where the narrower velocity resolution probe A has a lower current. Further, even with a finer velocity resolution probe, more sophisticated data analysis techniques are generally required to analyze broad-beam ion source data, like the HET, because the IVDFs of different species overlap. These data analysis techniques are described in detail in Section VI.

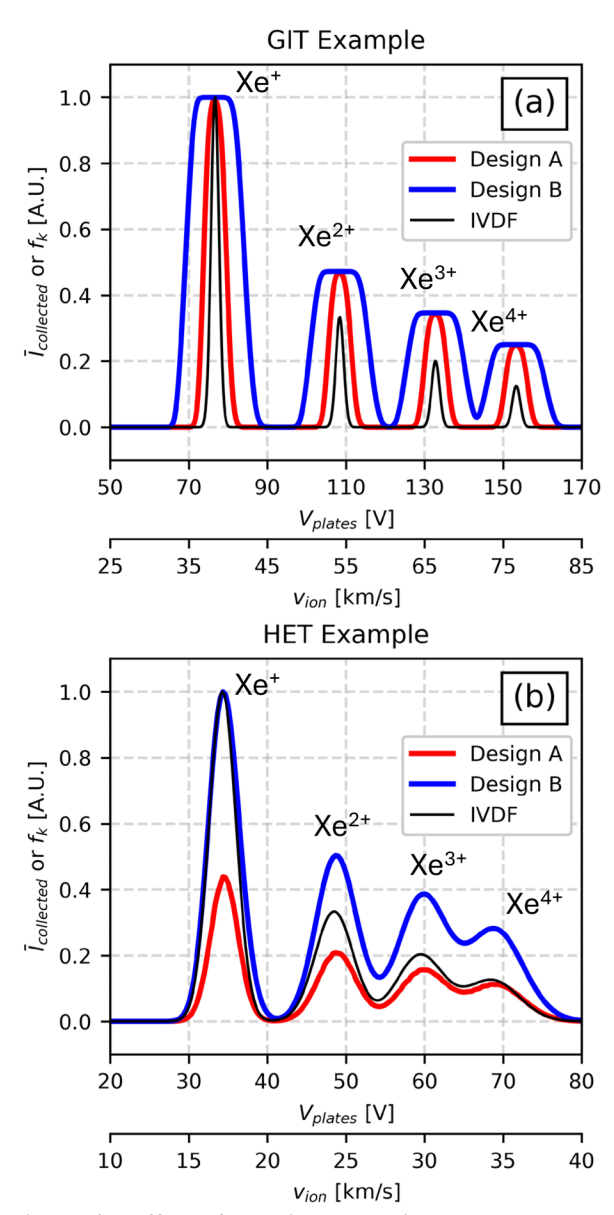


Figure 4: Effect of velocity resolution on the measured ExB probe spectra.

D. Transmittancy

The filtering properties of the composite ExB probe can be modeled and analyzed by considering it as a blur filter with an associated transmittancy. Figure 5 shows the concept of transmittancy. A single-species, monoenergetic ion beam enters the filter region from the left. In this case, the ion beam is deflected downward by a distance Δy_f because the ion velocity is slightly less than the Wien velocity. Even though the ion velocity is different than the Wien velocity, the measured current is not zero because a fraction of the beam still reaches the collector. The measured current is proportional to the fraction of the ion beam current that is transmitted and reaches the collector. The transmittancy and the convolution matrix of a specific probe geometry can be obtained analytically [57] or computationally by Monte Carlo simulation of the trajectory of ions through the instrument [59]. Figure 3 shows the transmittancy matrix computed for two notional probe designs. The figure shows that for a given value of the Wien velocity (v_W) , the transmittancy of a specific ion velocity (v_{ion}) is between 0 and 1, because anywhere between 0 to 100% of the ions with that velocity are transmitted through the probe.

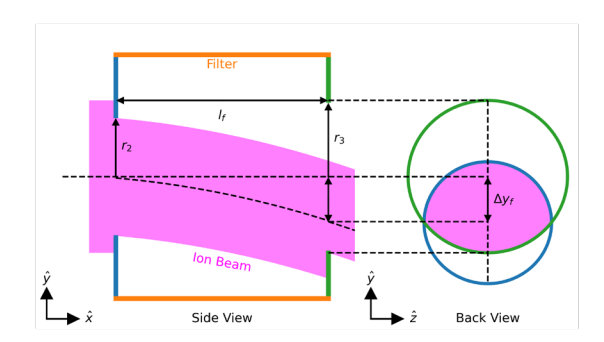


Figure 5: Illustration of transmittancy that is the fraction of the ion beam transmitted from probe entrance orifice to collector.

The effect of transmittancy on the measured ExB probe spectrum can be modeled. The ExB probe analyzes a population of charged particles whose velocity is described by a velocity distribution function, f, and for a particle species, k, the true IVDF of those particles is f_k . Ions with velocity that is different than the Wien velocity may still reach the collector (transmittancy is not zero) and the ExB probe counts these ions as ions at the Wien velocity. Therefore, the ExB probe acts as a blur filter of the true IVDF. The current collected at a given plate potential, and corresponding Wien velocity, for ion species k is given by:

$$I_k|_{V=V_{plates}} = A_{beam,k} q_k n_k \int_0^\infty [T_k(v, v_{Wien}) \cdot v f_k(v)] dv$$
 14

where $A_{beam,k}$ is the unfiltered beam diameter and n_k is the number density of species k. T_k is the transmittancy and is a geometric parameter of the probe. The transmittancy has a value from 0 to 1 and acts as a weighting factor in the convolution matrix.

The output data from the ExB probe, i.e., the ExB probe spectrum, can be interpreted as a convoluted image of the true IVDF. The measured probe current can be represented as Eq. 15, where $g_k|_{v=v_{Wien}}$ is the measured distribution function of the velocity v_{Wien} . Equations 14 and 15 together then form the convolution relation for the ExB probe, which reduces to Eq. 16. The measured probe spectrum (g_k) is modified from the true IVDF (f_k) dependent on the probe transmittancy (T_k) . With numerical regularization techniques it is possible to recover the true IVDF from the measured probe spectrum when the probe transmittancy is known. These data analysis techniques are described in Section VI.

$$I_k|_{V=V_{plates}} = A_{beam,k} q_k n_k v_{Wien} g_k|_{v=v_{Wien}}$$

$$g_k = \frac{v_{ion}}{v_{wien}} T_k f_k$$
16

IV. Design

Designing an ExB probe requires balancing resolution, signal strength, mechanical complexity, and environmental robustness. Higher velocity resolution is generally achieved through smaller entrance and exit apertures, longer Wien filter and drift sections, and tighter geometrical tolerances. These changes reduce the geometric transmission constant *G*, improving resolution as shown in Eqs. 12 and 13, but they also decrease ion transmission and collector current, which in turn lowers signal-to-noise ratio and may strain detection electronics. The resolving power of the probe is highly sensitive to its geometry—including collimator dimensions, filter length, and suppressor aperture size—all of which determine the range of ion trajectories that reach the collector. Crucially, the ExB filtering relies on strict orthogonality between the ion velocity, electric field, and magnetic field vectors; thus, precise alignment between the entrance collimator and the Wien filter is essential. Misalignment can introduce deviations from the ideal force balance and degrade velocity filtering. In practice, optimizing resolution must be weighed against practical constraints on probe size, manufacturability, and signal detectability. This section outlines recommended design practices for each major component of the probe, including guidance on materials, geometry, and practical tradeoffs related to signal quality and measurement fidelity.

A. Examples of Specific ExB Probe Designs

Figure 6 shows photographs of examples of specific ExB probes found in the literature and in use by the authors. In all the photographs, the collimator tube can be seen on the left, the Wien filter is in the middle, and the drift tube and detector are the tube on the right. Some designs are "bare" ExB probes (Figure 6a through f) where the collimator, filter, and drift tube are the exterior plasma-facing surfaces of the probe. Other designs enclose these components within a box such that the box is the exterior plasma-facing surface (Figure 6g and h). Further, some probes (Figure 6g and h) include a secondary electron emission (SEE) suppression electron between the drift tube and collector.

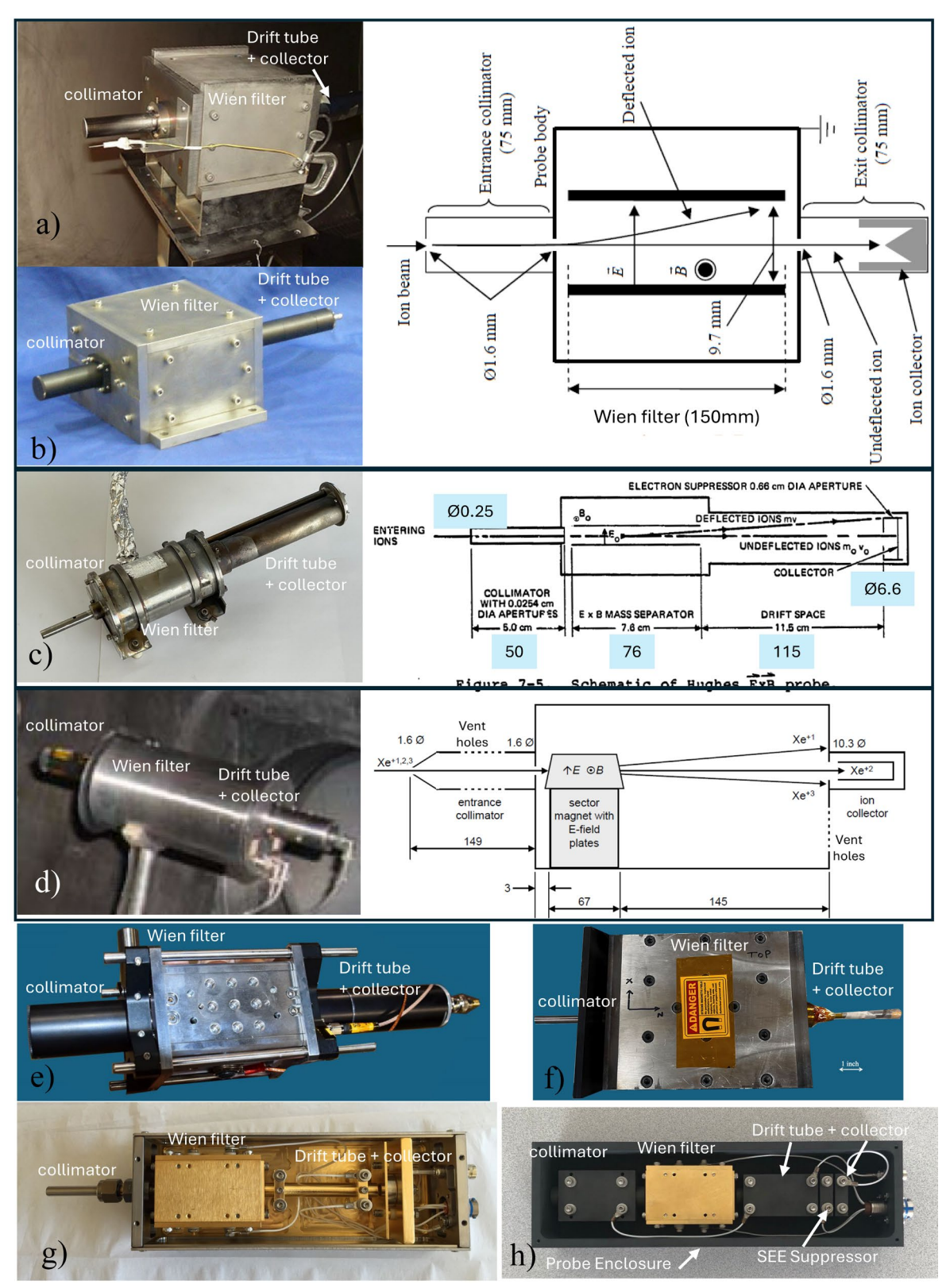


Figure 6: Photographs and schematics of ExB probes reported in the literature; a) and b) from Reid, et. al. [47] in use at University of Michigan and Georgia Tech, respectively, c) Vahrenkamp [33] and Beattie [60], d) Pollard [37], e) Naval Research Lab, f) University of Illinois dual-collector probe [61], and g) and h) Plasma Controls LLC. Units in mm.

B. Design Considerations for Specific Probe Components

1. Collimator

The collimator acts as a mechanical filter, limiting ion acceptance to those entering at small angles relative to the probe centerline. This ensures accurate velocity filtering and minimizes the impact of off-axis ions. The maximum acceptable incident angle is given by Eq. 17. To prevent contamination from thermal electrons, the entrance aperture radius should be smaller than the local Debye length $(r_1/\lambda_d \ll 1)$. Additionally, longer collimators improve angular filtering, but reduce signal due to geometric constraints.

$$\alpha_{max} = \tan^{-1} \left(\frac{r_1 + r_2}{l_c} \right)$$
 17

2. Wien Filter

The Wien filter is the core velocity selection mechanism of the ExB probe. It consists of two parallel electrodes that generate an electric field and two permanent magnets that produce a transverse magnetic field. These fields are oriented orthogonally to one another and to the ion velocity vector. The electrodes must be electrically isolated from the rest of the probe. Symmetric plate biasing is recommended to minimize field distortion, and electrode geometries should be optimized to reduce edge effects. The magnetic field is typically generated using permanent magnets, with the body of the filter designed to help guide and shape the field. High-uniformity fields can be achieved using a k=2 Halbach array configuration.

For the filter electrodes, stainless steel or molybdenum are commonly used, with gold plating optionally applied to maintain electrical conductivity and prevent oxidation in humid environments. The housing that supports the electrodes and magnets may either contribute to magnetic field shaping or serve as a passive structural element. If field shaping is desired, soft magnetic materials such as low-carbon steel or magnetic stainless (e.g., 430SS) can be used to guide the magnetic flux. In designs where the magnetic field is self-contained, such as with a Halbach array, non-magnetic materials like graphite or aluminum are suitable alternatives, offering lower sputter yields and simplified machining. For electrical isolation, high-temperature ceramic insulators such as alumina, steatite, macor, or boron nitride are recommended due to their dielectric strength and thermal resilience. Polymeric insulators like PEEK may be used in low-temperature environments.

Permanent magnets must maintain their magnetic field strength under elevated temperature conditions typical of EP testing. Common choices include samarium-cobalt (SmCo), neodymium-iron-boron (NdFeB), and ceramic magnets. SmCo is often preferred for its superior thermal stability. Field strength is typically in the range of 0.15 to 0.4 Tesla.

3. Drift Tube and Collector

The drift tube connects the Wien filter to the collector and provides space for velocity-based deflection to occur. A longer drift length increases the ion trajectory separation, thereby improving resolution. However, longer tubes also reduce transmitted current and increase probe size.

The collector serves as the detection element of the ExB probe, measuring the ion current that passes through the filter and drift sections. Ion induced electron emission (IIEE) can artificially inflate measured current. The IIEE yield, sometimes referred to as ion-induced secondary electron yield (IISEY), depends on several factors, including ion species, charge state, and kinetic energy, as well as properties of the target material such as work function and surface condition [62-64]. IIEE is often divided into potential and kinetic components. The potential electron emission is independent of projectile energy and attributed to Auger or resonance neutralization. In contrast, the kinetic emission is energy-dependent and occurs via direct momentum transfer from the projectile. It dominates at keV energies but can sometimes contribute below 1 keV. To reduce IIEE, the collector is typically made from materials with low secondary electron yields, such as molybdenum or tungsten, where molybdenum is easier to machine. The IIEE yield of molybdenum and tungsten under xenon bombardment is given in Table 2. The ion current measured for each species can be expressed including SEE as Eq. 18, where γ_k is the SEE yield for species k at the ion energy of interest.

$$I_k = q_k n_k v_k A_c \left(1 + \gamma_k \right) \tag{18}$$

Table 2: IIEE yield for xenon ion bombardment of common collector materials in electrons per ion [65-67].

Xenon Charge State	Molybdenum	Tungsten
1	0.022	0.016
2	0.20	0.20
3	0.70* est. from W	0.71

To mitigate IIEE from the collector, a combination of geometric and electrical suppression techniques is typically employed. One common approach is to shape the collector using a cone-in-cylinder geometry that helps recapture emitted electrons. This geometry for the collector is shown in the schematic of the probe of Figure 6a and b. Additionally, a suppressor electrode may be implemented just upstream of the collector and biased slightly negative, typically in the range of -20 to -30 V, relative to the (usually grounded) collector. This negative bias repels secondary electrons and prevents them from escaping the collector region. This approach is shown in the probes of Figure 6g and h.

The ion current signal can be in the low pA range downstream of typical thrusters, particularly off axis. Earlier ExB probe designs often employed electron multipliers (e.g., a channeltron) to boost the signal-to-noise ratio when high-sensitivity detection electronics were not readily available. Many recent measurements have instead relied on shielded signal transmission using coaxial or triaxial cables and a low-noise amplifier, for instance a picoammeter or electrometer.

4. Other Considerations

The housing should be made of materials with low sputter yield and high thermal tolerance. Graphite is often used due to its durability and low sputter rate. To protect sensitive components from thermal loads, a grounded graphite or similarly heat-tolerant thermal shield may be installed in front of the probe.

In low-conductance probes, especially those with narrow apertures and long collimators, neutral gas can accumulate. This may affect measurement fidelity due to charge exchange (CEX) reactions within the probe volume. Vent holes may be utilized to prevent pressure buildup and can be protected with fine metal mesh to avoid plasma ingress.

Alignment of all probe components is key. A common mechanical approach to aid alignment is the use of gauge pins or dowel pins inserted through precision-machined alignment holes to maintain coaxiality between components like the collimator and Wien filter. Typically, the pins are inserted during assembly to hold parts in place while fasteners are tightened, and then removed prior to operation to avoid mechanical over-constraint, interference with thermal expansion, or electrical issues. In setups where sub-millimeter alignment is required, optical alignment methods—such as using laser beams projected through apertures—can help verify probe orientation relative to the thruster centerline or specific plume features.

V. Implementation and Operation

This section describes the recommended electrical and mechanical setup and operation of the probe in an EP test facility. Additionally, recommendations on the probe motion or sweep through the thruster plume and the pointing and orientation of the probe with respect to the thruster are also described. Recommendations regarding probe field-of-view, alignment, and check-out procedures are also provided.

A. Electrical Setup

An ExB probe has at its core a velocity filter containing orthogonal electric and magnetic fields. Typically, the magnetic field is held constant with permanent magnets while the plate voltage is adjusted to impose an electric field of varying strength and thereby adjust the filter band-pass velocity. The ions that pass through the filter collide with a collector electrode and are recorded as current. Thus, the base electrical configuration of the ExB probe should allow for (1) adjusting the electric potential difference between two plates (V_{plates}) to establish the electric field and (2) precise collection and measurement of ion current at the collector. Considerations regarding power supply biasing, probe body biasing, and current collection are essential to ensure precise and accurate probe measurement and operation.

Data analysis generally requires curve-fitting to the recorded data. The resolution and range of V_{plates} potential difference values investigated must be sufficient to enable the data analysis. Generally, it is recommended to set the range of V_{plates} values by first estimating the V_{plates} value required to detect the highest charge-state specie, and then add an extra 50%. Thus, the recommended minimum plate voltage range ($V_{plates,range}$) is given by Eq. 19 [68]. A

general estimate of V_{accel} is 75-97% of the discharge voltage for Hall-effect thrusters [45,69]. $V_{plates,range}$ should be calculated for each expected species charge-state, and the most conservative (largest) value should be used. For example, for the probe in Figure 6A, the $V_{plates,range}$ used during HET testing is typically 0 to 120 V. The resolution of the V_{plates} setpoints is typically on the order of 1 V.

$$V_{plates,range} = \left[0, 1.5 \sqrt{\frac{2eZV_{accel}(d_eB)^2}{m}}\right]$$
 19

The recommended electrical configuration for the bare and enclosed E×B probes are shown in Figure 7A and B, respectively. An important consideration that drives this electrical configuration is the fact that the probe is immersed in plasma and therefore there exists a plasma sheath at all surfaces exposed to plasma. For the bare probe, the collimator, filter, and drift tube external surfaces are exposed to plasma, while the enclosed probe has a box surrounding those components and they are not in direct contact with the plasma. In either case, an incoming ion must pass through the sheath to enter the probe and this can result in an additional accelerating force if the electric potential of the external plasma is different than the internal probe potential [52]. With this in mind, it is recommended to ground the probe body or enclosure box that is in contact with the plasma. While floating the chassis should result in even less mismatch with the plasma potential, grounding arguably provides superior electrical shielding against noise.

Any biasing (including grounding) of the probe body or enclosure affects the plasma sheath. For example, as probe body or enclosure potential decreases, the sheath expands and disturbs the local plasma environment and can thereby affect ion trajectories entering the probe and the band-pass velocity [43]. Hence, it is important to measure the local plasma potential at the entrance of the probe, which can be accomplished using a Langmuir [5] or emissive probe [6]. But, generally, the plasma potential in the plume at the probe location is only a few volts above facility ground (e.g., 3-15 V) and this is small compared to the typical beam energy (100-1000 V), so any ion energy/velocity gain between plasma potential and ground is small and typically neglected.

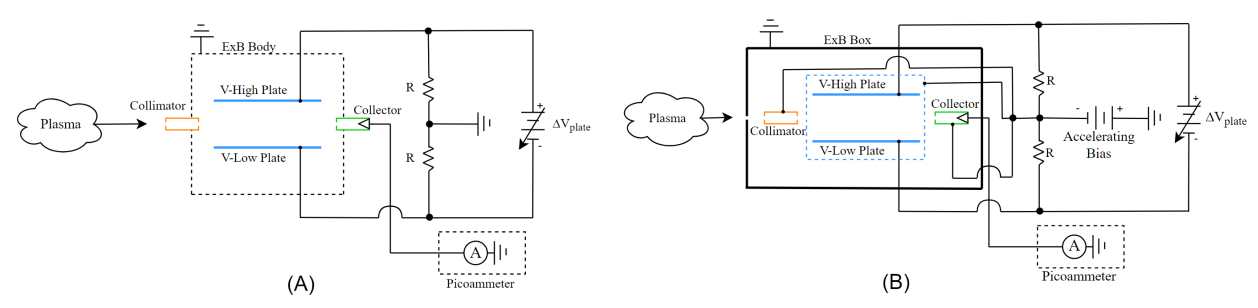


Figure 7: Recommended ExB probe electrical configuration: (A) bare and (B) enclosed probe, respectively.

In the case of the bare probe of Figure 7A, it is recommended to also set the probe interior centerline potential to ground potential. To achieve this, it is recommended that the two plate electrodes be symmetrically biased such that the centerline potential is zero. That is, the electrodes should have the same electric potential magnitude, but one electrode should be positive potential with respect to ground and the other negative. This is achieved using a grounded voltage divider circuit on the supply voltage (as shown in Figure 7). The voltage divider resistances, R, should be equal and are recommended to be in the hundreds of $k\Omega$ to $M\Omega$ resistance range to minimize leakage current.

This same grounded-centerline-potential approach can be taken for the enclosed probe of Figure 7B. However, in this case, since the probe body is not in direct contact with the external plasma, it can be biased negatively relative to the enclosure. This allows ions to accelerate in the gap between the enclosure and the collimator entrance orifice, thus increasing the ion velocity (Eq. 6) and correspondingly the Wien velocity at which the ion transmits through the probe. This is shown by Eq. 19, where V_p is the plasma potential and V_{accel} is the magnitude of the negative accelerating bias potential. Essentially, the accelerating potential increases the separation between the plate voltages for each m/q species in the measured ExB spectra.

$$v_{w,k} = \sqrt{v_w^2 - \frac{2q_k}{m_k} \left(V_p - V_{accel}\right)}$$
 20

The capability to accelerate ions immediately before they enter the probe has important benefits for studies on low energy ion populations, such as charge exchange ions and ion beams with multiple species with similar mass-to-charge ratio (e.g., air) [70]. An example of this is shown in Figure 8 for a notional low-energy air ion beam. There are four possible ion species: O_2^+ , O_2^+ , O_2^+ , and O_2^+ , which have mass-to-charge ratios of 32, 28, 16, and 14 amu/q, respectively. All species are assumed to have beam most probable energy of 20 eV. Because of the relatively low energy and small separation in mass-to-charge ratio of these species, the probe is unable to resolve all four species, and the measured probe spectrum has only two distributions: diatomic and monatomic species. When an accelerating bias potential of 280 V is applied, the distributions shift to higher Wien velocity (v_w or plate voltage $V_{electrodes}$) in the measured probe spectrum. Further, the two distributions bifurcate and now show the presence of two diatomic and two monatomic species.

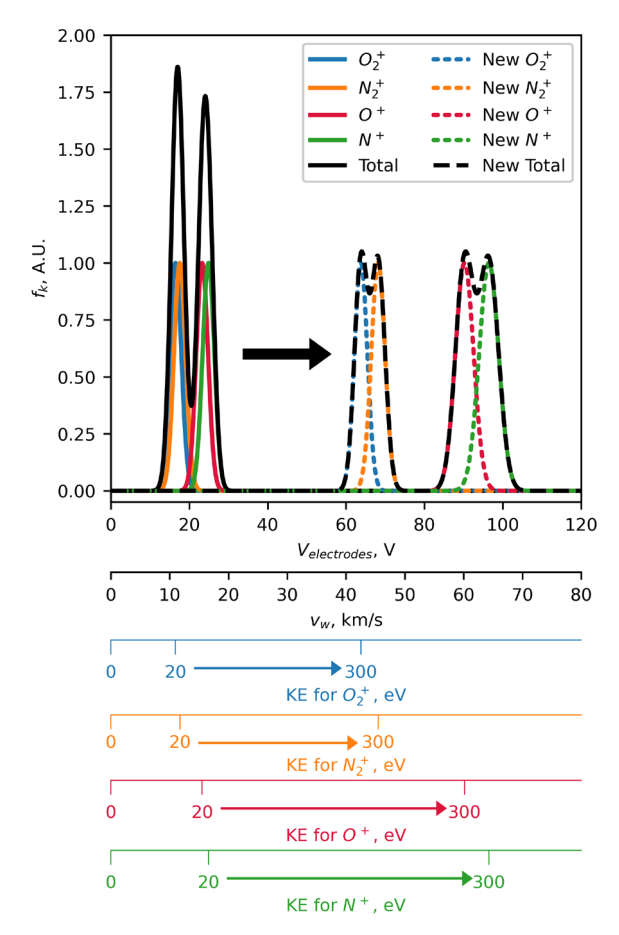


Figure 8: Applying an accelerating potential to ions entering the ExB probe shifts the spectrum to larger Wien velocity and separates the distributions of species with similar mass-to-charge ratio.

It is important to mitigate plasma interactions and ambient noise within the probe to ensure accurate current measurements and a high signal-to-noise ratio. Internal to the E×B device, the plates and collector surface should possess strong isolation, both from each other and from probe body. Typically, these components are mounted on ceramic structures, or other structures of high dielectric properties, and the electrical connections are routed to avoid contact to a conductive surface. To minimize spurious particle scattering in the probe, only low-outgassing materials should be used. If the probe body is properly grounded, the electrical connections internal to the E×B probe can either route via wire or coaxial cable with a low risk of signal interference. The maximum current that reaches the collector is a function of the E×B geometry, operational plume current density, and plume species composition, but is typically on the order of tens of picoamperes to nanoamperes [43,46,47,52,58,68]. To maintain a clean and accurate signal with these low currents, special attention must be placed on the collector wires and current measurement device. It is recommended to use grounded shielded wire to transport the collector current and a picoammeter to measure the

current as its current measurement range aligns with the operational range of most E×B configurations. Figure 9 is a photograph of the electrical connections to the ExB probe shown in Figure 6A.

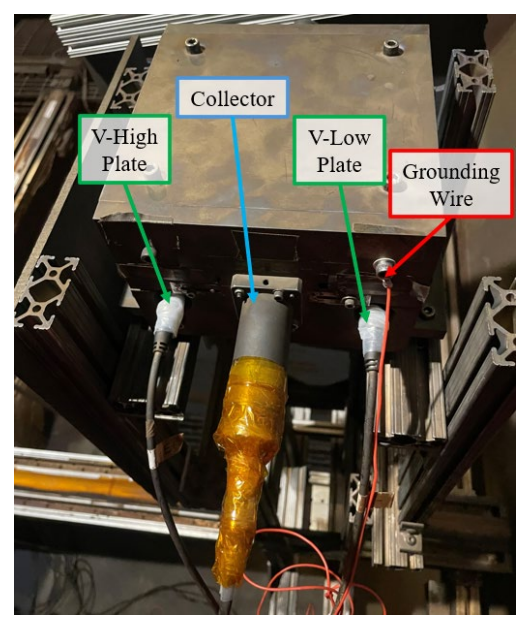


Figure 9: Electrical connections of probe shown in Figure 6A.

B. Physical Setup

The basic setup is an ExB probe placed downstream of and in the plume of the thruster test article, inside a high vacuum test facility. The probe may either be stationary or attached to a motion stage, co-located with additional plasma diagnostics or isolated. When developing the test geometry and sweep routine for the probe, one must consider thermal issues and signal strength, probe alignment, type of thruster, and type of data one hopes to gather.

1. Thermal and Sputter Erosion Issues

For applications involving high-power thrusters or when the ExB probe may be exposed to high level of thermal energy, it is recommended that the probe be installed with a protective shield. This shield should also be designed to minimize sputter erosion by energetic ions, which can produce contamination that backstreams onto the thruster. One approach is to place a low sputter-yield graphite plate or sheet metal with graphoil between the probe and the thruster. This shield should have minimal area to reduce the absorption of thermal power and be mounted with thermal conductive materials (e.g. not stainless steel) to an ambient or cooler surface to ensure it does not overheat. The use of a shutter to protect the entrance of the probe may also be warranted depending on application. If a protective shield is used, ensure that the protective shield is conductive and electrically tied to the same electrical plane as the entrance collimator of the ExB probe (e.g., electrically tie both components to facility ground). If the shield is at different electric potential than the entrance collimator (10+ eV), the resulting electric potential gradient can lead to abnormal behavior in the signal measured by the probe, leading to erroneous results. A conical shield or entrance aperture can also redirect sputter products away from the thruster.

For high-power application, the temperature of the ExB probe should be monitored to ensure any permanent magnets in the probe do not exceed their operating temperature limit. Note that operating temperature limit of permanent magnet is when the magnet strength begins to degrade, which is lower than the temperature when the magnet experiences permanent demagnetization (a.k.a. the Curie temperature). For reference, an ExB probe, protected by a thermal shield, that was swept at 1.5 m from a 12-kW thruster over ~1 hour experienced approximately 20-25 °C increase in temperature. After a full day of testing (~8 hours of sweeping), the ExB probe temperature reached around 50-60 °C. The key to keeping the probe cool is to make sure the heat on the thermal shield is effectively carried away from the vicinity of the probe.

2. Probe Alignment

The ExB probe requires precise line of sight alignment to the thruster to ensure sufficient signal to noise ratio and proper collection of the desired ion species. One alignment method to ensure proper probe alignment is to use an

alignment laser to adjust the ExB position. With this method, the collector is removed from the rear of the ExB probe and an alignment laser is replaced in the collector position. The ExB apertures are then adjusted to maximize the laser transmission through the probe and the probe is positioned to project the alignment laser on the thruster area of interest. Figure 10 illustrates the alignment laser projection process while aligning the ExB probe to the centerline of the P5 thruster.

If the thruster is attached to a motion stage, one must ensure the probe remains aligned to the desired target position or positions throughout the range of motion. Misalignment can occur if the axes of the motion stages do not line up properly with the appropriate axes of the thruster (e.g. centerline, plane of the thruster face, etc) or the probe is not pointing completely orthogonal to the appropriate axis of motion (e.g. an axis of rotation). The vertical alignment can be verified by placing a horizontal laser level at the height of the target and ensuring laser passes through the centerline of the front and the back of the probe over the range of motion. For a polar angle probe sweep with a fixed target on the face of the thruster, the horizontal alignment can be verified by placing a vertical laser level across the face of the thruster and ensuring the laser passes through the centerline of the probe when it is at +90° and -90°.

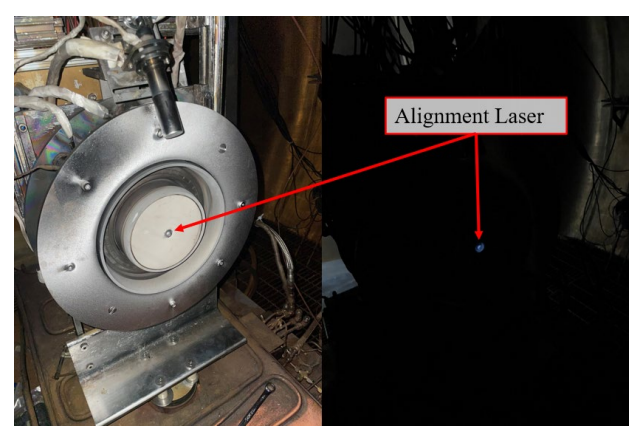


Figure 10: ExB laser alignment to centerline of the P5 Hall effect thruster.

3. Field of View Considerations and Recommendations

The ExB probe is highly sensitive to orientation angle because of its collimating inlet. Consider the ExB described in Ref. [37]. It has an acceptance angle of 0.6° , resulting in an 8 mm viewing spot on the propulsion device face at distance of 82 cm. If this probe is on the thruster axis, this spot drifts 14 mm across the face of the thruster for each degree of misalignment. Hence a small shift in alignment could change where, or if, ions are being sampled from the thruster. This is in stark contrast with many other plasma probes used for characterizing EP devices. For example, a Faraday probe may be angled up to 8° from optimum orientation, such that it is not even pointing at the thruster, and only lose 1% of its current collection area.

It is possible to increase the ExB field of view either by reducing the ExB collimation or by increasing the distance of the probe. The former decreases the ExB velocity resolution, eventually interfering with charge state analysis. The latter is limited by test chamber geometry and can result in increased systematic effects due to charge-exchange between the thruster and the probe.

Accepting that the field of view may be smaller than the thruster face, it is natural to ask where on the thruster should the field of view be positioned and located. This depends greatly on the geometry of the thruster being interrogated. Careful alignment of the probe to a pointing angle that provides the strongest and most representative signal is critical.

Test Geometries for Gridded Ion Engines

Sensible test geometries for a large, gridded ion engine are well documented (e.g. [37,71]). For example, the setup used by Pollard et al. [37] to interrogate the NEXT engine is shown in Figure 11. The key is that the probe should always point normal to the grids while in the central region of the ion beam and maintain a fixed distance, d, from the grids. This ensures it will capture the maximum current of each beamlet within its field of view. As shown in Figure 12A, for flat grids, this is achieved by mounting the probe to a linear stage orthogonal to the thruster face and sweeping the field of view from the left grid edge to the right grid edge. As shown in Figure 12B, for dished grids this is achieved by mounting the probe to a rotating arm with its axis of rotation at the radius of curvature R of the grids. Sweeping across the face of the grids provides charge state information useful for determination of thruster efficiency. If one is

instead concerned with plume composition in the periphery (e.g. to determine erosion rates on peripheral surfaces), one must adopt a different test geometry. In this case the probe should be swept about an origin on the thruster face while maintaining pointing at that origin. Previous studies found that the empirical origin of high angle ions was predominantly from the near edge of the grids for a convex dished ion engine [37,71]. An example of this geometry is shown in Figure 12C. Other thrusters may have that origin closer to the center.

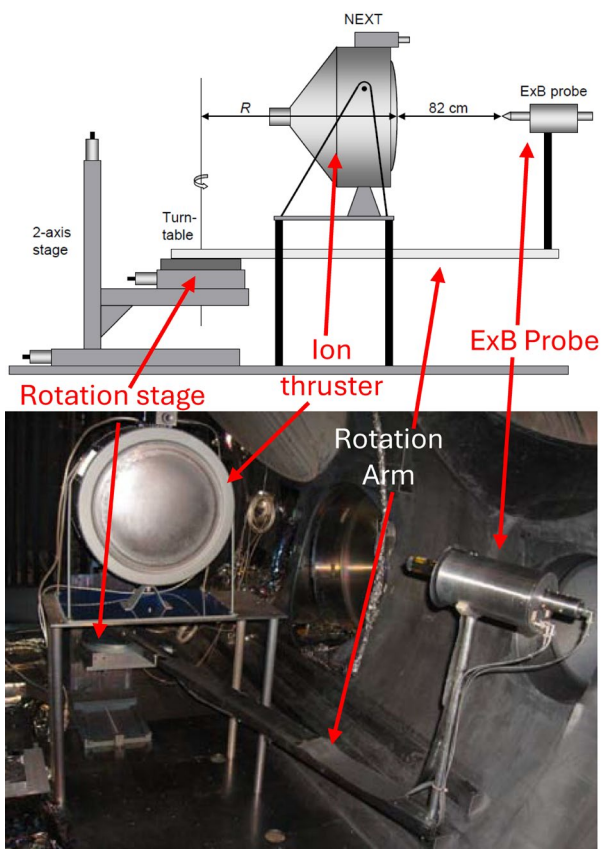


Figure 11: Schematic and photograph of example ExB probe setup for ion thruster plume measurements. Reproduced with permission from [37].

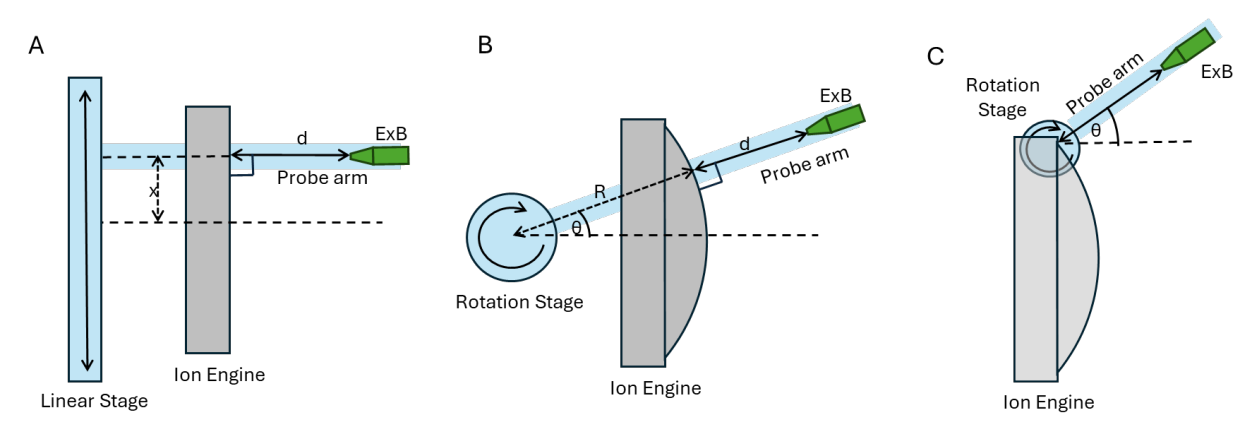


Figure 12: ExB probe position and single-axis motion with respect to different ion engine grid geometries.

An even more ideal setup would allow fine tuning of the pointing angle for each polar angle to maximize overall signal. Figure 13 shows a few two-axis test geometries that allow for such tuning. Such geometries may also allow measurement of charge-state both in the central plume and periphery. Note that each geometry imposes different conditions on angular range and involves variable probe distances.

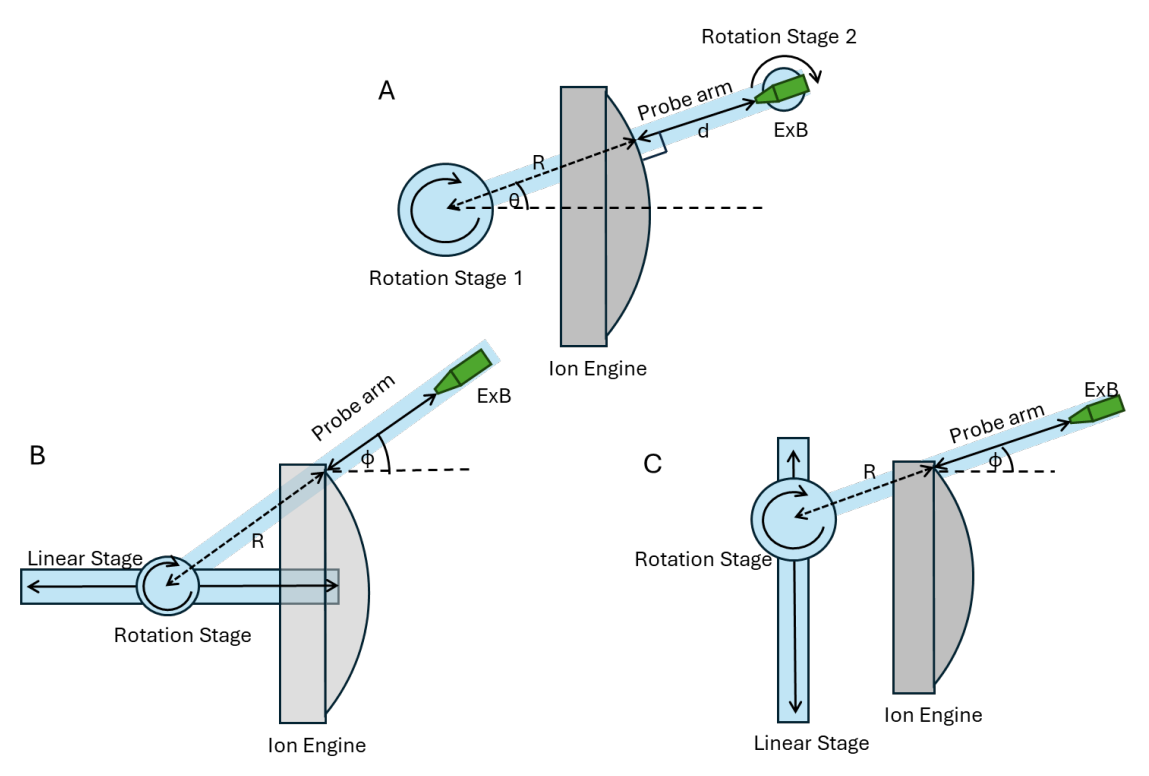


Figure 13: Example ExB probe locations and two-axis motion for ion engine testing.

Test Geometries for Hall Thrusters

The test geometry used for Hall thrusters in previous literature is typically the center of the thruster or the channel. The former seems to be dictated more by convenience as one typically mounts an ExB alongside a variety of other probes with broad view factors and comparatively insensitive orientation requirements. For an annular Hall thruster, the true origin of the accelerated ions is not the thruster centerline, but the annular channel surrounding it (technically the acceleration region may extend somewhat beyond the channel). This was demonstrated by Sullivan et. al. [48], where they scanned an ExB probe across the thruster face at different polar angles relative to the thrust axis and found two distinct signal peaks associated with the near and far channels. They also found evidence of a "central jet" with apparent origin at the center of the thruster, but only for very low angles (e.g. <10°). At many angles, if the ExB probe is not sampling from the channel, it is not getting a representative measurement of charge state for the majority of the beam.

Fast ions can be assumed to travel in straight lines in field-free, low-density regions. However, some curvature of those paths is expected in the near-field of the thruster. Hence, the line-of-sight field-of-view of the ExB is slightly different from the true field-of-view, accounting for ion curvature. Empirically, this may result in the optimally aligned ExB probe having a line-of-sight to slightly different locations on the thruster face for each polar angle.

Figure 14 shows one suggested geometry for Hall thruster measurement. For extra tuning, a linear stage to provide transverse displacement of either the thruster or the pivot arm is suggested. This has the added advantage that it allows collocation of additional probes referenced to thruster centerline on the same arm as the ExB probe.

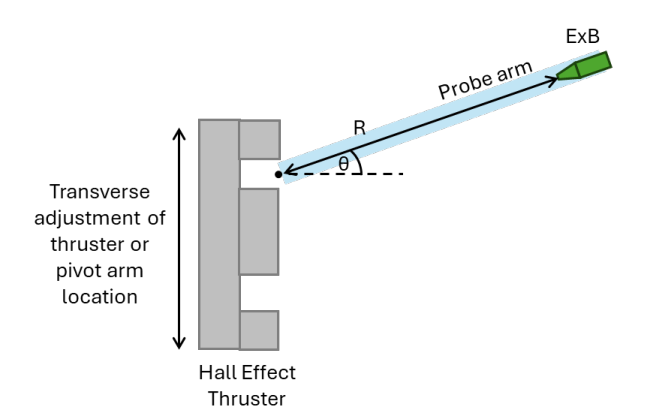


Figure 14: Example test setup geometry for Hall thruster testing.

These test geometry setups use some in-situ motion of the probe or thruster that is accomplished by rotational and/or translational motion stages. Off-the-shelf motion stages can be prone to lose alignment at vacuum and low temperatures. It is recommended to ensure there is an in-situ method to maintain alignment of motion stages. This can include motion encoders or home switches, visual alignment within the frame of a fixed camera, or alignment with laser marker.

C. Recommendations for Interrogating a Hall Thruster Main Plume and Side Plume

Any given Hall thruster will exhibit at least two ion populations with very different characteristics. They are typically called the beam ion population, which has energy near the discharge potential, and the CEX ion population, which has energy around tens of eV. Note that while most CEX ions are created from interaction of beam ions with facility background neutrals, some CEX ions are created from interactions of beam ions with thruster neutrals and will be present even in space. In many Hall thrusters, particularly magnetically-shielded Hall thrusters, one or more ion populations of medium energies (typically 100 to 200 eV) have also been observed [72,73]. Each of the aforementioned ion populations have different points of origin and trajectories, and will exhibit higher or lower signal strength depending on where the ExB probe is placed relative to the thruster and what direction the probe is pointed at.

Typically, the region within +/- 45 degrees of the firing axis of a Hall thruster is called the main plume or main beam as the plasma in this region is dominated by the beam ion population. The region outside of the main plume is sometimes referred to as the side plume, and non-beam populations including CEX and medium energy ions dominate. The angles that define the transition from main plume to side plume varies with thruster and tends to be larger for operating conditions with lower discharge voltage (60-80 degrees from the firing axis for 300 V discharge) and smaller for operating conditions with higher discharge voltage (40-60 degrees from the firing axis for 600 V discharge). Within the transition region, the overlap between competing ion populations can render accurate analysis of the data difficult to impossible. Figure 15 shows ExB probe data taken at four different angles relative to the firing axes of a thruster operating at 600 V, 12.5 kW [74]. This probe was pointed at radial center of the thruster exit plane. Notably, beam ions dominate the data at 0 and 30 degrees from the firing axis with a medium energy population starting to appear at 30 degrees. In the same figure, CEX and medium energy ions dominate the data at 60 and 90 degrees from the firing axes.

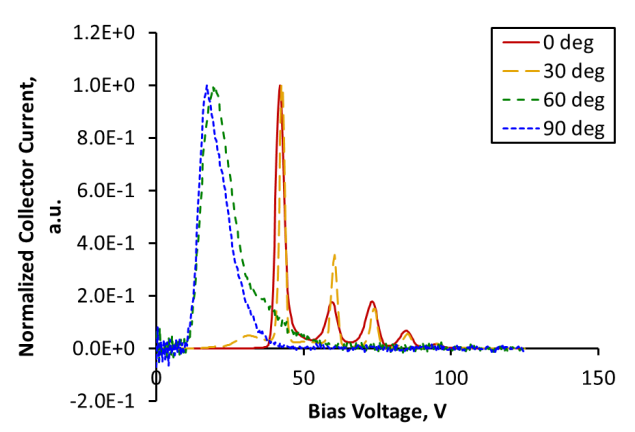


Figure 15: ExB probe data taken at four different angles relative to the firing axes of a thruster operating at 600 V, 12.5 kW [74].

When using ExB probe to characterize the contributions of multiply-charged species to thruster inefficiencies, the measurements should focus on the main plume, as they are responsible for >90% of the thrust generated. If measurements are made from beyond approximately 4 times the mean diameter of the discharge channel, the probe can usually be aimed at the center of the channel at the exit plane and achieve sufficient signal-to-noise ratio (SNR). Note that questions remain as to whether data collected in this manner will always be representative of the majority of ions originating from the discharge channel, particularly outside the central jet region [48]. If possible, the superior approach is to find the pointing angle at each polar angle where signal is maximized. This is expected to occur when the discharge channel falls within the acceptance angle of the probe. If measuring from closer than 4 times the mean diameter, the probe may need to be aimed at the center of the discharge channel to achieve sufficient SNR.

When using the ExB probe to characterize the contributions of multiply-charged species to erosion of the thruster and/or spacecraft, the measurements should focus on the side plume, as ions velocities that are mostly tangential to the firing axis are responsible for most of the plume-induced erosion. The distance at which these measurements are made depends on the focus of the characterization (e.g., measurements supporting spacecraft wear analysis should be beyond 4 times the mean diameter of the discharge channel). When measuring the side plume, it may be necessary to aim the ExB at a location downstream of the exit plane as many CEX and medium energy ions appear to be born downstream of the exit plane.

D. Pre-test Checkouts

Certain specific probe checkouts are recommended to limit measurement uncertainty in the data collection process and reduce the resultant systematic uncertainty. Probe checkouts can be categorized into electrical and operational checkouts, and are recommended prior to operating the ExB probe. For the electrical checkouts, it is imperative that the following surfaces are isolated from each other and from ground: (1) Collector, (2) V-High Plate, (3) V-Low Plate, (4) Electron Suppression Grid (if installed). If the probe design includes a grounded enclosure (shield) with biased internal probe body, the elements of that body, including collimators, test section, and drift section should be electrically continuous with each other while isolated from ground. The signal shields and enclosure should be in physical contact with each other and electrically connected to a common ground. If the probe design requires a fully grounded body, the probe body components and shielding should be continuous and in physical contact with each other and connected to a common ground.

The operational checkouts consist of measuring the magnetic field along centerline and centerline gap distance to ensure there are minimal degradations to the probe, and if any deviations from standard measurements exist, the updated values should be used for probe data processing. The permanent magnets in the ExB probe may degrade over time, either due to excessive probe heating close to the Curie temperature, chemical or physical events causing a change in the magnetic microstructure, or time-based magnetic creep [75,76]. Thus, it is recommended to measure the magnetic field strength on probe centerline with a Gauss meter prior to each use to quantify any degradations. Similarly, having an accurate measurement for the gap spacing between the electric field plates in the ExB probe is important since this spacing directly affects the strength of the produced electric field. Periodically measuring and recording this gap distance will ensure there are no shifts over time in the plate positioning and produced electric field strength.

VI. Data Analysis

Over the decades, electric propulsion researchers have developed a variety of approaches to analyzing Wien filter data, some of which are device specific. For ion thrusters, peak height analysis is common because it is a narrow beam source and so a wide resolution ExB probe can be used. The resulting probe data tend to have well-separated non-overlapping peaks corresponding to each charge state. An example ion thruster ExB probe data set is shown in Figure 4A. For the Hall thruster, which is a broader beam source, the most common approach is to perform some form of integration of the data while assuming a particular form for the velocity distribution function. This is often done with a variety of corrections depending on the level of fidelity that the user is trying to achieve. There is a tradeoff between minimal effort and fidelity for the different data analysis methods and the user is advised to weigh the tradeoffs. For example, a user developing a new Wien filter for a laboratory that is likely to be used for ten years may opt to spend the upfront effort to develop an automatic data analysis script that achieves a high level of accuracy. Whereas a user working with data in a one-off application without detailed knowledge of the probe may forego some correction factors that are effort intensive to implement. In all cases, the user should try to estimate the uncertainty in the final results associated with the fidelity of analysis performed.

A. IVDF Reconstruction

The recorded ExB probe spectrum is a convolution of the true IVDF, as described by Eq. 16. An estimate of the true IVDF can be reconstructed from the measured ExB probe spectrum and the inverse of the convolution matrix, as described by Eq. 21 (bold text indicates matrices).

$$f_k = T_k^{-1} g_k \tag{21}$$

The convolution matrix of the ExB probe may not have an inverse or may be ill-conditioned. In this case the problem can be viewed as a linear inverse problem as shown in Eq 22, where ϵ represents noise or errors in the measured data. Simply trying to solve Eq 22 using a least squares technique can lead to unstable solutions. Regularization helps by imposing additional constraints that lead to more stable and realistic solutions. The most common form of regularization is Tikhonov regularization [59,77-79], which adds a penalty on the size of the solution. The modified minimizing function is given by Eq 23, where λ is the regularization parameter. The solution can be obtained analytically as Eq 24.

$$\boldsymbol{g}_{k} = \boldsymbol{T}_{k} \boldsymbol{f}_{k} + \boldsymbol{\epsilon} \tag{22}$$

$$g_k = T_k f_k + \epsilon$$

$$\min_{f_k} (\|T_k f_k - g_k\|^2 + \lambda \|f_k\|^2)$$
23

$$f_{k,est} = (T_k^T T_k + \lambda I)^{-1} T_k^T g_k$$
 24

The regularization parameter must be chosen to balance the fit and the smoothness of the data. Larger value of λ smooth the solution more, but may underfit the data. There are a number of mathematical discussions on the regularization techniques [80]. The iterative Tikhonov regularization method has been used in a prior application of ExB probe in Hall thruster [59]. Figure 16 shows an example of the IVDF reconstruction technique. The synthetic probe spectrum from ExB probe B of Figure 4B is used here. The cyan dashed line represents the IVDF reconstructed from synthetic ExB probe spectrum via the iterative Tikhonov regularization technique. By applying the regularization technique, the IVDF was reconstructed from the measured spectra. After the IVDF has been reconstructed, the current and species fractions can be determined using the techniques described next.

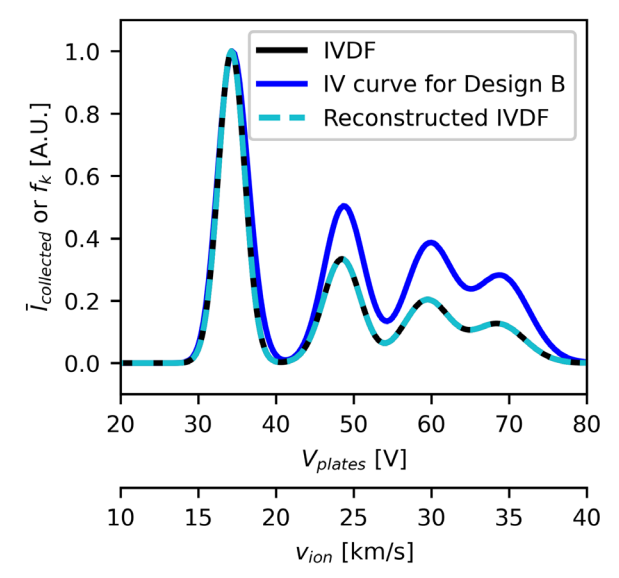


Figure 16: Example of the reconstruction of the IVDF from the ExB probe spectrum of Figure 4B.

B. Calculating Current and Species Fractions

The most basic information obtained from an ExB probe is the current and species fraction. Various analysis methods for deriving these quantities in a Hall thruster setting are described here, roughly in order of increasing effort.

1. Peak height

The simplest method for analyzing Wien filter data is to assume that the height of each peak is equal to the relative amount of current associated with each species. Assuming a single propellant and all charged species undergo roughly the same potential drop, the peak associated with the lowest probe bias should be the singly-charged species, the peak with the next higher bias should be the doubly-charged species, and so on. Further, the peaks should be separated by a ratio of the square root of the charge state (i.e., higher charge states are at higher plate potential difference, as described by Eq. 8). Once the relative current fraction of each species is calculated, the species fraction can be approximated using Eq. 25 [81], where ζ_j is the species fraction of the j-th species, and Z_i is the charge of the j-th species.

$$\zeta_j \approx \frac{\Omega_j / Z_j^{3/2}}{\sum_i \Omega_i / Z_i^{3/2}}$$
 25

If multiple propellants are present and the potential drop experienced by each propellant are roughly the same, all singly-charged species of each propellant should be separated by a ratio of the inverse of the square root of atomic mass (i.e., the lighter ions of a given charge show up at higher plate potential difference, as described by Eq. 7). The remaining description assumes a single propellant unless otherwise specified.

The peak height method is very simple to code and avoids the complexities associated with areas of the data where the distributions of different species overlap. While it may be an acceptable analysis approach for ion thrusters under specific conditions, it has been shown to be highly inaccurate for Hall thrusters [58,81]. A sample ExB probe trace illustrating the peak height analysis method is shown in Figure 17. The data were collected using the Advanced NEXT gridded ion engine; details of the thruster design, test facility, and operating conditions are provided in Ref. [82]. The probe design shown in Figure 6h was used, with the probe swept radially at a fixed axial distance of 82 cm downstream of the accelerator grid, as illustrated in Figure 12b. Charge-exchange effects were addressed using the method described in Section VI.C., resulting in corrections of approximately 5% depending on the operating condition and background pressure. The doubles-to-singles current ratio was calculated to be 0.18 for the shown trace. The spatially resolved signals were analyzed using the peak height method and numerically integrated to determine the multiply charged ion thrust correction factor, which has previously been shown to closely align with independent thrust stand measurements [83].

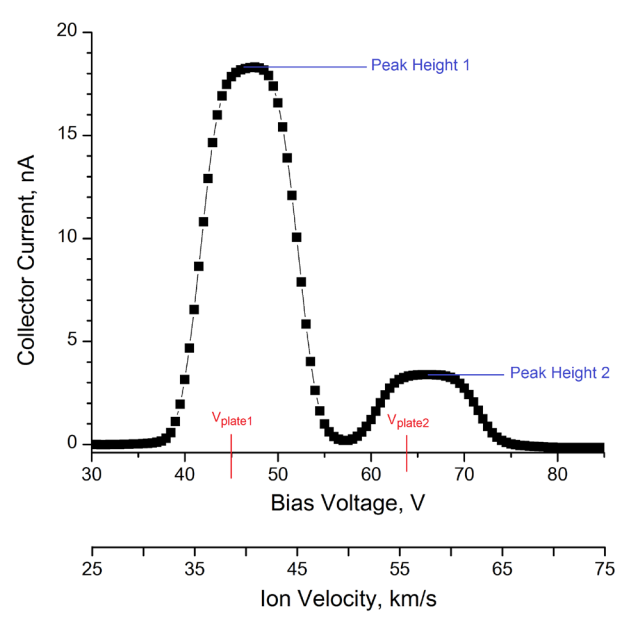


Figure 17: ExB probe trace acquired on centerline of the Advanced NEXT engine at a beam voltage of 1068 V and beam current of 6.0 A. The measured peak locations show good agreement with the predicted values (V_{plate1} , V_{plate2}) from Eqn. 8.

2. Simplified integration

Another method for analyzing ExB probe data is to assume that the area under the curve associated with each peak is the total current of the corresponding charged species. This method will be referred to as "simplified integration". If the peaks are clearly separated and there is no floating offset in the data, simplified integration can be used. However, Hall thruster plume ions are generally not clearly separated and floating offset can be difficult to avoid. Generally, one must assume a form for the IVDF and perform the appropriate curve-fit prior to integration. A variety of IVDFs have been used in past literature [42,84-86] and the common forms are shown in Eqs. 26-30. They are, in order, triangle, Gaussian, variable exponent, twin/bi Gaussian, and skew-normal distributions. In these equations, f_j is the distribution function of the j-th species, and a, b, c, d, n, a_1 , b_1 , c_1 , a_2 , b_2 , and c_2 , are fitting constants. The erf[] term refers to the error function. The form of the IVDF commonly employed by the authors in their research is skew-normal or twin/bi Gaussian.

Triangle:
$$f_{j}(v) = \begin{cases} (-a/b)|v-c| + a, c-b < v < c+b \\ 0, else \end{cases}$$
 26
Gaussian:
$$f_{j}(v) = a \exp[-b(v-c)^{2}]$$
 27
Variable Exponent:
$$f_{j}(v) = a \exp[-b|v-c|^{n}]$$
 28
Twin/Bi Gaussian:
$$f_{j}(v) = a_{1} \exp[-b_{1}(v-c_{1})^{2}] + a_{2} \exp[-b_{2}(v-c_{2})^{2}]$$
 29
Skew-Normal:
$$f_{j}(v) = a \exp\left[-\frac{(v-c)^{2}}{2b^{2}}\right] \left\{1 + erf\left[-\frac{d*(v-c)}{\sqrt{2b^{2}}}\right]\right\}$$
 30

Once a form is selected and fitted to the ExB probe data, Eq. 31 can be used to calculate the current fractions by performing the integrals shown, where I_j is the probe current for species j, and V_{plates} is the potential difference across the probe plates. Assuming all charged species undergo roughly the same voltage drop, Eq. 31 can then be used to calculate the species fraction. The integration approach presented in this section assumes the velocity resolution is a constant function of probe plates bias voltage, which is physically incorrect as shown in Section III.C. However, the results are a good approximation so long as the peaks are narrow and all charged species undergo roughly the same potential drop.

$$\Omega_{j} = \frac{\int_{0}^{\infty} I_{j}(V_{plates}) dV_{plates}}{\sum_{j} \int_{0}^{\infty} I_{j}(V_{plates}) dV_{plates}}$$
31

As an example, Figure 18 shows a typical data fitting procedure for the simplified integration method. The ExB spectrum was acquired on the NASA 300-M thruster operating at 500 V, 20 kW on xenon propellant using the probe shown in Figure 6D. Figure 18A is the raw measured probe spectrum and shows the measured current as a function of the plate electrodes bias voltage. This spectrum has four distinct peaks corresponding to each xenon charge state. To start the analysis, in Figure 18A, the DC offset is subtracted. The DC offset is calculated most commonly by one of three methods. In each method, an average of the current is taken when no (or very little) ions are impacting the collector. The methods are (a) averaging current from the beginning and end of trace, (b) averaging current at the end of the trace only, or (c) averaging over a null trace (thruster off). In the example shown in Figure 18, option (a) is utilized. An average of the collected current over the range $20 > V_{plates} > 90$ is calculated and subtracted from the spectrum. The two averaging windows are shown in Figure 18A between each set of grey vertical lines. This offset is largely the result of instrument noise and is often ignored during data analysis.

Next, each of the four distributions are sequentially fit with a Bi-Gaussian. In each case, the bounds are user-selected. This fitting process typically starts with the lowest charge-state, Xe^+ , and subsequent fits to higher charge-states are done after removing (subtracting) the fit(s) from the prior lower charge-state(s). The fitting bounds for each charge state are shown as vertical lines in the figure, and the curve fits for singly-, doubly-, triply-, and quadruply-charged xenon are shown in Figure 18B, C, D, E, respectively. The residual indicates the difference between the raw current measurement and the curve fit. Again, note that when fitting to a given charge-state, the residual for it and lower charge-states is near zero because the curve fit(s) for it and the lower charge-state(s) has been subtracted from the raw current measurement. A summation of the four Bi-Gaussian distributions is shown in Figure 18F and compared with the raw measured current. In this case, the fit and the raw current are in close agreement, highlighted by a R^2 value close to unity. The R^2 value, at least in principle, is a good metric to check whether the assumed IVDF shape (Bi-Gaussian) and fitting windows were properly selected for the data. Current and species fractions are calculated using the four Bi-Gaussian distributions fit to the data and Eqs. 25 and 31, respectively. These values are given in Table 3. Note that CEX corrections have not been made for these data (to be discussed in Sec. C).

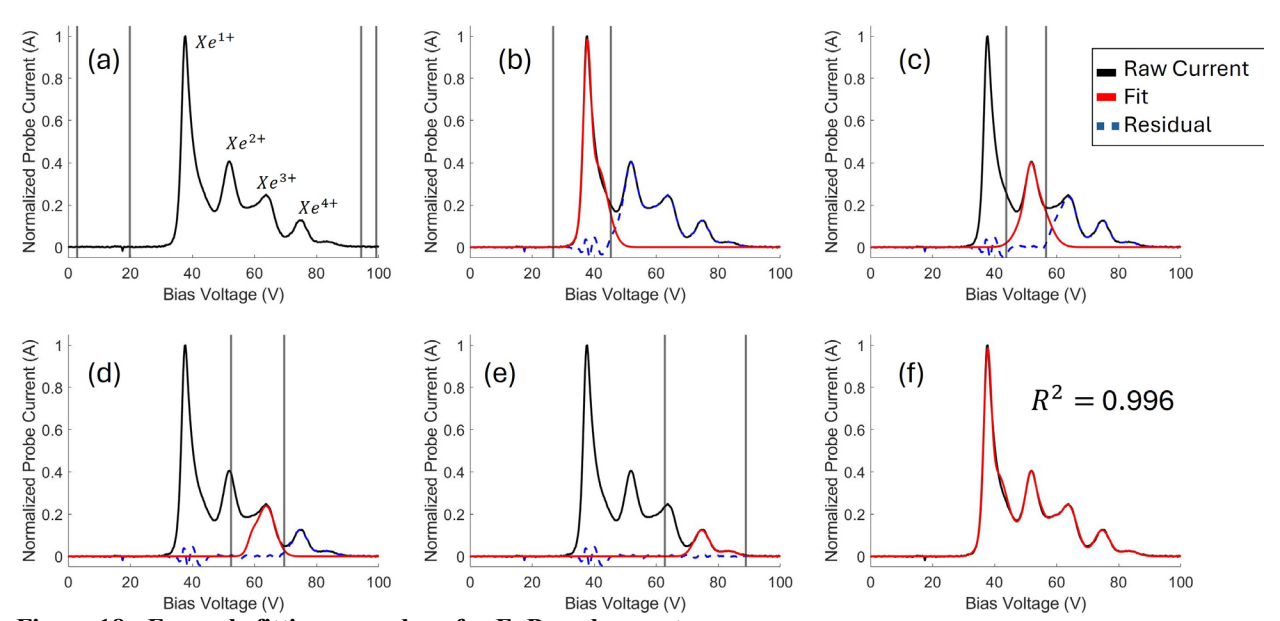


Figure 18: Example fitting procedure for ExB probe spectra.

Table 3: Current and species fractions calculated from the data of Figure 18.

Species	Current	Species				
эрестев	fraction (Ω)	fraction (ζ)				
Xe ⁺	0.48	0.78				
Xe^{2+}	0.24	0.14				
Xe^{3+}	0.19	0.06				
Xe^{4+}	0.09	0.02				

3. Advanced integration

In an idealized ExB probe, the maximum deviation in velocity that a particle can have from the Wien velocity (v_{Wien}) and still make it through to the detector scales as square of the Wien velocity (Eq. 12) [58]. The Wien filter velocity scales with applied probe plates bias for a given strength of magnetic field, accounting for the probe resolution means that an additional V_{plates}^2 term is needed in the integration. This integration approach will be referred to as "Advanced integration". Specifically, after a curve-fit form is chosen, Eq. 32 is the actual form to be fitted to the data, where K_1 and K_2 are probe-specific geometric constants and n_i is the absolute density of the j-th species. Since K_1 and K₂ are probe-specific geometric constants, they will cancel out when calculating relative current and species fractions. In theory, it is possible to calculate the absolute density if K_1 is known, but this is difficult for most practical devices and is not necessary for deriving relative current and species fractions.

$$I_{j}(V_{\text{plates}}) = K_{1} n_{j} V_{plates}^{3} f_{j}(K_{2} V_{\text{plates}})$$
32

When the curve-fit constants are found, Eqs. 33 and 34 can be used to calculate the current and species fractions, respectively [58]. Assuming all charged species undergo roughly the same voltage drop, Eq 25 can also be used to calculate the species fraction from the current fraction. In practice, using Eq 25 instead of computing the integral (Eq. 34) introduces error that is negligible relative to other sources for data from Hall thrusters operating at 300 V or more. If uncertain, it is recommended to compute the integral for a few representative cases as a check. Assuming the IVDFs are narrow and all charged species undergo the same potential drop, it is possible to show that Eqs 31 and 33 reduce to the same result [58]. In practice, for Hall thruster plasmas, the simple integration of area under the curve and integration with idealized probe resolution differs by at most a few percent. The difference tends to be larger for ion beams with wider IVDFs.

$$\Omega_{j} = \frac{I_{j}}{\sum_{j} I_{j}} = \frac{Z_{j} \int_{0}^{\infty} \frac{I_{j}(V_{plates})}{V_{plates}^{2}} dV_{plates}}{\sum_{j} Z_{j} \int_{0}^{\infty} \frac{I_{j}(V_{plates})}{V_{plates}^{2}} dV_{plates}} dV_{plates}$$

$$\zeta_{j} = \frac{n_{j}}{\sum_{j} n_{j}} = \frac{\int_{0}^{\infty} \frac{I_{j}(V_{plates})}{V_{plates}^{3}} dV_{plates}}{\sum_{j} \int_{0}^{\infty} \frac{I_{j}(V_{plates})}{V_{plates}^{3}} dV_{plates}} dV_{plates}$$
34

$$\zeta_{j} = \frac{n_{j}}{\sum_{j} n_{j}} = \frac{\int_{0}^{\infty} \frac{I_{j}(V_{\text{plates}})}{V_{plates}^{3}} dV_{plates}}{\sum_{j} \int_{0}^{\infty} \frac{I_{j}(V_{\text{plates}})}{V_{plates}^{3}} dV_{plates}}$$
34

Figure 19 is a set of bar graphs that compare the current fraction results using the simplified versus the advanced integration method with the skew-normal IVDF form [58]. Figure 20 is a set of bar graphs that compare the current fraction results using the advanced integration method with different IVDF forms for three representative throttle points of the NASA-300M. Also shown are the results the peak height method [58]. Note that all results shown in Figure 19 and Figure 20 are after correction for charge exchange effects. In general, the results show that the advanced integration method is more accurate while requiring a bit more effort to code. Since the integration is not a simple area under the curve, verification using simple shapes or against prior data should be performed to ensure the code is performing the integration properly.

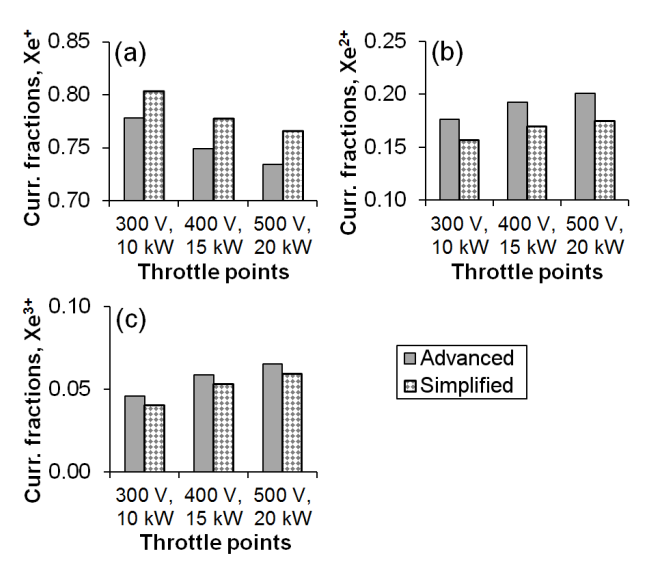


Figure 19: Comparison of current fraction results between the simplified and advanced integration methods. Reproduced from [58] with permission.

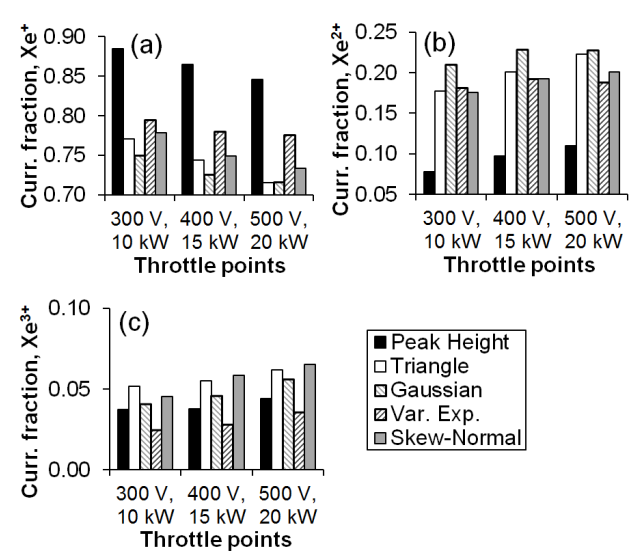


Figure 20: Comparison of current fraction results using the advanced integration method with different IVDF forms of Eqs. 26-30. Reproduced from [58] with permission.

4. Bayesian fit

Instead of using curve-fits, users can implement Bayesian inference techniques to fit the ion population. When appropriately implemented, this method avoids ambiguities associated with user selected bounds for each fitting window and provides a more systematic and robust approach to fitting the data. To perform Bayesian fit, the Wien filter spectra, f_{ExB} , can be defined as the sum of the IVDFs for each individual ion species f_k as shown in Eq. 35.

$$f_{ExB} = \sum_{k} f_k(\theta)$$
 35

In this formulation, θ represents the model fitting parameters. For example, a single population spectrum that is assumed normally distributed would have three fit parameters: $\theta = \mu, A, \sigma$. In Bayesian inference, the model parameters are distributions that are updated after introducing data, d, through Baye rule as shown in Eq. 36.

$$P(\theta|d) \propto P(d|\theta)P(\theta)$$
 36

Here, $P(\theta|d)$ is the posterior distribution of model parameters, $P(d|\theta)$ is the likelihood function, and $P(\theta)$ is the prior distributions. The likelihood function, or model, is the summation of the assumed IVDFs for each species. The prior distribution for each parameter represents the state of knowledge before introducing the data. Selection of the prior is the most subjective part of Bayesian inference but can be a useful tool to dis-allow unphysical parameter values. For example, negative values for the intensity, A, or the variance, σ , in a gaussian distribution can be avoided by specifying a uniform prior U(0-x).

For ExB probe spectra, most assumed IVDFs will be non-linear, requiring the use of techniques like Markov-chain Monte Carlo to sample from the un-normalized posterior distribution $P(\theta|d)$ [87]. For each posterior sample, the area under the curve method, Eq. 31, or advanced integration techniques, Eqs. 32 and 33, should be used to evaluate the current fractions. After evaluating the current fractions for each sample, statistics like the mean, maximum a-posteriori, and variance can be inferred from the result. These statistics provide estimates for both the species current fractions and fit uncertainty. Automatic uncertainty analysis is one primary advantage of Bayesian inference over the sequential fitting methods. This can be particularly helpful when there is significant distribution overlap, and the location of peaks is ambiguous [88]. ExB probe uncertainty analysis is discussed further in Section VI.D.

C. Correction for Charge Exchange Effects

Regardless of the exact method for deriving the current and species fractions, ExB probe data obtained in most ground test environment must be corrected for CEX effects. The effect of charge exchange with background neutrals is typically corrected by modifying the integrated current and integrated density. The correction scheme for Xenon propellant, shown in Eqs. 37-39, was first presented by Shastry, et al. [81]. In these equations, J is the current density a distance z away from the thruster exit plane, J_o is the current density at the thruster exit plane, and n_o is the average background neutral density. The ion energy per charge, V_1 , V_2 , and V_3 for Xe^+ , Xe^{2+} , and Xe^{3+} , respectively, are either measured by another probe (e.g., a retarding potential analyzer) or assumed to be equal to the discharge voltage. Using the discharge voltage instead of measurements for V_1 , V_2 , and V_3 typically introduces <1% systematic error for ExB probe data that are taken on or near the thruster firing axis [81]. In other situations, an uncertainty analysis should be performed to characterize the error. The value of n_0 is typically calculated from facility pressure readings from ion gauges [1].

$$(J/J_{0})_{1} = exp(-n_{0}\sigma_{1}z), \quad \sigma_{1} = [87.3 - 13.6 \log(V_{1})] \times 10^{-20}m^{2}$$

$$(J/J_{0})_{2} = exp(-n_{0}\sigma_{2}z), \quad \sigma_{2} = [45.7 - 8.9 \log(2V_{2})] \times 10^{-20}m^{2}$$

$$(J/J_{0})_{3} = exp(-n_{0}\sigma_{3}z), \quad \sigma_{3} = [16.9 - 3.0 \log(3V_{3})] \times 10^{-20}m^{2}$$

$$\Omega_{j}^{C} = \frac{\Omega_{j}[(J/J_{0})_{j}]^{-1}}{\sum_{j=1,2,3} \Omega_{j}[(J/J_{0})_{j}]^{-1}}$$

$$40$$

Equation 40 is used together with the correction factors in Eqs. 37-39. The term Ω_j^C denotes the corrected current fraction of the j-th species and Ω_j is the uncorrected current fraction determined from Eq. 31 or 33. Species fraction can be corrected in the same manner. Prior works have shown that asymmetric charge exchange (e.g., $Xe^{2^+} + Xe \rightarrow 2Xe^+$) can be neglected for Hall thruster application [81].

D. Uncertainty Analysis

1. Uncertainties in the measurement system

In an appropriately designed ExB probe system, probe and electronics uncertainties are typically not the driver of the overall uncertainty. However, these uncertainty factors should be characterized and minimized to ensure they do not drive the overall measurement uncertainty of the system. The energy resolution of the probe represents the lowest achievable measurement uncertainty contributed by the ExB probe itself. This factor was described in detail in section III.C. Another source of probe uncertainties is any misalignment introduced during the construction of the probe. This is typically a negligible source of uncertainty when using modern machining techniques.

All electronics have measurement uncertainties described in their respective manufacturing specifications. ExB probe system typically rely on accurate nanoampere or even picoampere meters. These low-current meters are susceptible to thermal drift. If their thermal drift characteristics have not been characterized by the manufacturer, then they should be characterized to ensure their contribution to total uncertainty is low. If custom components are used (such as external shunts, trans-impedance amplifiers, etc.), the entire measurement electronic system should be characterized together to determine the overall system uncertainty. For example, one can attach a precise current reference (such as a calibrated sourcemeter) to the input of the measurement electronic system and check how the

measured value changes over time and as ambient temperature changes. The rate of change combined with time between calibration and typical range of ambient temperature can then be used to determine whether the electronics uncertainty is a driver of the overall uncertainty.

2. Uncertainties in data analysis

The two primary sources of uncertainty in the data analysis for ExB spectra are a) overlapping velocity distribution functions, and b) charge exchange correction factors. Overlapping IVDFs can lead to a large uncertainty in the relative current/species fractions. The degree to which the species overlap is a function of both thruster type and operating condition. For example, in ion thrusters and non-magnetically shielded Hall thrusters, the distributions are typically distinct. In contrast, magnetically shielded Hall thrusters, especially at high discharge current densities, typically exhibit significant distribution overlap.

An example of distribution overlap is illustrated in Figure 21, which is an example ExB probe spectra from a magnetically shielded Hall thruster at two different operating conditions. The degree of overlap can vary, ranging from easily discernable peaks at low current (Figure 21a) to strongly convoluted at high current (Figure 21b). When the saddle point between distributions is clear, as in Figure 21a, Huang et. al. [58] devised a method to estimate the maximum uncertainty through geometric arguments. While this conservative approach is sufficient in most cases, when the location of saddle points is ambiguous (c.f. Figure 21b), other methods must be used. The preferred method to estimate uncertainty in cases of significant IVDF overlap is to implement a Bayesian fitting approach. As outlined in section VI.B.4., using Bayesian inference techniques to learn the distributions avoids ambiguity of user selected bounds, and statistics like the variance provide automatic uncertainty quantification [88].

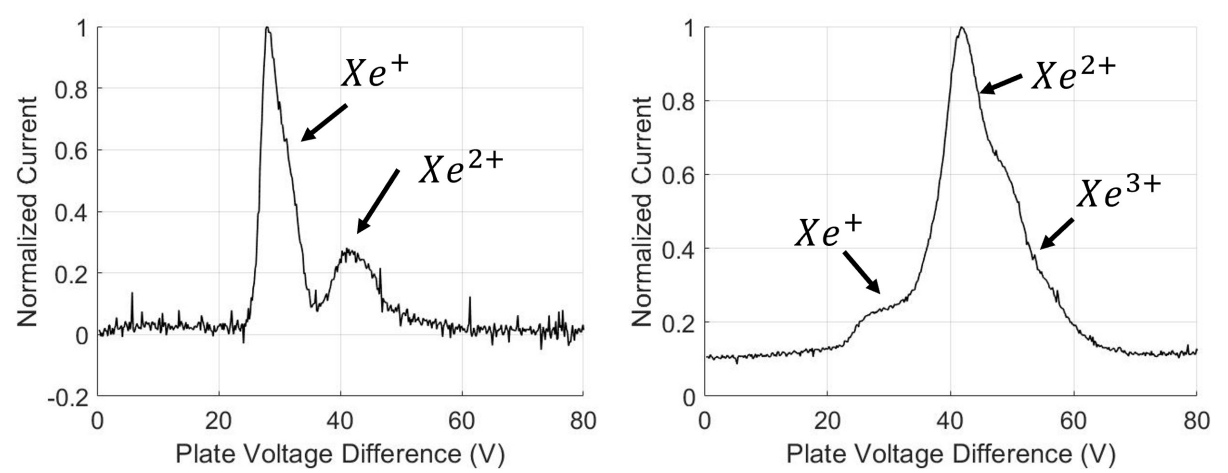


Figure 21: ExB spectra from the H9 magnetically shielded Hall thruster operating on xenon at a) 300 V, 15 A and b) 300 V, 100 A [88]. These data were acquired with the ExB probe of Figure 6A.

In addition to the overlapping IVDFs, there can be significant uncertainty associated with the CEX correction of raw integrated current fractions. As discussed in section VI.C., different CEX collision cross sections for each ion species with the background neutral gas changes the beam composition at the entrance of the ExB probe compared to immediately downstream of the thruster exit plane. The key inputs to the correction model (Eqs. 37-39), are the CEX collision cross section, σ , the distance of the ExB probe, z, and the background neutral density, n_0 . Of these three inputs, the dominant uncertainty source is the estimate of background neutral density, n_0 . Background neutral density is typically calculated from pressure measurements made with ionization gauges with a typical uncertainty of 10-20%. Further, the calculation may be an underestimate because ion gauge measurements are typically made at a lower pressure region at or near the vacuum test facility wall [1], which is outside the high density plume region where ions are having CEX collisions. The CEX correction model assumes a constant background neutral density along the flight path from the thruster to the ExB probe. In reality, the neutral density is non-uniform and likely decreases an order of magnitude within 1 m downstream on thruster centerline. Analysis by Shastry et. al. [81] demonstrated that under most situations where the probe is located far from the thruster (many thruster diameters), CEX attenuation of the beam ions is dominated by collisions with neutrals from the facility background rather than neutrals from the thruster. However, if the probe is placed close to the exit plane (a few thruster diameters) then it is likely that the thruster neutral pressure cannot be neglected and may dominate. Compared to background neutral density, the uncertainty of the other two inputs is negligible. Collision cross section only depends on the ion energy in a logarithmic fashion, and the distance to the ExB probe can be measured precisely, rendering these uncertainties negligible.

Focusing on the uncertainty in background neutral density, the uncertainty in current fractions can be determined from Eq. 41. Following the analysis of Huang et al. [58], the partial derivative of Eqs. 37-40 are taken with respect to neutral density and the CEX correction uncertainty is propagated to the current fraction estimate. The result is Eq. 41 and, in this formulation, δn_0 is the uncertainty in the neutral pressure.

$$\left(\frac{\delta\Omega_j^C}{\Omega_j^C}\right) = (n_0 z)^2 \left[\sum_{k \neq j} (\sigma_j - \sigma_k) \Omega_k^C\right]^2 \left(\frac{\delta n_0}{n_0}\right)^2$$
 41

VII. Comparison with Other Diagnostic Approaches

There are numerous other diagnostics commonly employed to characterize and interrogate the velocity and energy properties of particles in EP thruster plasmas and plumes. A summary of these diagnostics and relevant characteristics is given in Table 4. Retarding Potential Analyzer (RPA) and Electrostatic Analyzer (ESA) [8] are widely used plasma diagnostic probes for analyzing the ion energy distribution function (IEDF). The RPA operates as a high-pass ion energy filter by sweeping a voltage across a set of grids. It provides a cumulative IEDF, requiring users to numerically differentiate the measured data to obtain the energy distribution. In contrast, the ESA functions as a band-pass ion energy filter by sweeping a voltage between two electrodes, allowing ions with specific energies to reach the detector directly. This enables users to obtain the IEDF without additional data processing. While the ExB probe can separate particles based on their mass-to-charge ratio, both the RPA and ESA analyze energy per unit charge, meaning they cannot distinguish ions with different mass-to-charge ratios. This limitation can sometimes be advantageous, such as in double-layer plasmas. The RPA and the ESA offer advantages in their compact sizes and relatively simple constructions.

The Time-of-Flight (TOF) technique measures the ion velocity by determining the difference in arrival times of ions. It functions as a high-pass velocity filter, with the filter velocity varying as a function of time. To obtain the IVDF, users must differentiate the measured data. However, the species discrimination capability of the TOF techniques is generally inferior to that of the ExB probe, particularly when the density of minor species is significantly lower than that of major species. Another limitation of the TOF technique is its reduced effectiveness in time-varying plasmas when the plasma timescale is faster than the TOF device's operational timescale. While the TOF system can be constructed to be lighter than an ExB probe, its overall size is often comparable, as it requires a certain length to achieve optimal performance.

The Quadrupole Mass-Spectrometer (QMS) is a highly sensitive (can be <0.1 amu) mass filter for ions, which is often integrated into Residual Gas Analyzers (RGAs). In a QMS, four conductive rods are arranged parallel to the ion traveling direction. Two of the rods, maintained at positive DC and alternating RF potentials, function as a high-pass filter, while the other two, held at negative potentials, act as a velocity filter. A very narrow band-pass can be achieved by precisely tuning the amplitudes of the DC and RF potentials, as well as the RF time constant. This level of mass resolution is challenging for most ExB probes to replicate. However, the QMS's complex design and the high cost of commercial systems make it a less accessible option.

Laser-Induced Fluorescence (LIF) is an optical diagnostic technique used to determine the IVDF for a specific species. LIF involves directing a laser at a specific wavelength to excite particles (ions or neutrals) and detecting the light emitted as the particles spontaneously radiatively decay to their original energy state. By analyzing the emitted light, the VDF of the targeted species can be determined. A key advantage of LIF is that it is non-invasive, and the measurements can be done without significantly disturbing the plasma properties. Additionally, LIF can be focused on challenging regions, such as the inside of a Hall Effect Thruster (HET) channel. However, LIF has limitations, including a minimum detectable particle density determined by the sensitivity of the detector system. Furthermore, the technique requires lasers tuned to the specific wavelength(s) of the particular species being studied. As a result, LIF is typically applied to measure the IVDF of the dominant species in a plasma.

Table 4: Summary of characteristics for each velocity (energy) determination technique. Y as yes, N as no.

	ExB	RPA	ESA	TOF	QMS	LIF	EVADER
Typical Size/Mass	Large	Small	Medium	Medium	Large	Outside	Large
Can discriminate species?	Y	N	N	Y	Y	N	Y
Pass-band filter?	Y	N	Y	N	Y	Y	Y

Invasive?	Y	Y	Y	Y	Y	N	Y
Needs V_p correction?	Y	Y	Y	Y	Y	N	Y

Another recently developed diagnostic for interrogating ion beams is called the EVADER [89]. The EVADER diagnostic combines a spherical electrostatic analyzer (ESA) with a Wien-filter (ExB) stage in a single line-of-sight package. The instrument first filters ions based on their energy-per-charge (E/q) using the ESA sector. The narrow E/q beam exiting the ESA then enters the ExB probe where it is filtered based on particle mass-per-charge (m/q) ratio. For an ion beam where all the ions have the same mass, e.g., xenon ion beam, the EVADER provides a measure of the energy distribution of each charge-state species within the beam. Specifically, each ExB spectrum is recorded at a known, user-selected E/q band, so a sequence of spectra taken across the global ion energy distribution function (IEDF) can be stitched together to reconstruct species-specific IEDFs and current fractions. This type of probe was initially demonstrated by Thompson et. al., who used the probe to characterize a 1.5 kW krypton Hall thruster [89].

The motivation for this combined probe resulted from the observation that Hall-thruster plumes—and especially magnetically-shielded or high-current density operation—produce broad energy and species distributions that force the singly- and multiply-charged peaks in a conventional ExB probe spectra to overlap as shown in Figure 21b. Analyses that rely on peak heights or fitted IVDFs are then more susceptible to the assumed IVDF shape and fitting window. By pre-selecting a user-defined E/q band, the EVADER can remove much of the overlap before the ExB stage, so each spectrum contains better-resolved, less-convoluted peaks.

In the context of other diagnostic approaches, discussed above, for measuring energy, species, and velocity distributions, the EVADER retains the functionality of both an ESA and ExB probe, but with the added benefit of the reduced overlapping of velocity distributions collected in the ExB stage. The primary drawback of the probe is the added experimental complexity of the combined probe operation, relative to a standalone ExB or ESA. This includes an additional set of power supplies necessary for sweeping the effective E/q transmission band and the ExB probe plates, while measuring low nano- and picoamp currents at both the ESA and ExB collectors, respectively. Although the improved minor species sensitivity may surpass that of some TOF systems, the mass sensitivity is significantly coarser than that of a QMS. The EVADER bridges the gap between energy-filtering and velocity-filtering (mass-to-charge-filtering) diagnostics. By reducing peak overlap it provides reliable species fractions obtained in wide-energy EP plumes, while offering actionable, species-resolved IEDFs to inform performance, lifetime, and modeling efforts.

VIII. Conclusions

This paper presented recommended practices for the design, operation, and data analysis of ExB probes used in electric propulsion testing. The ExB probe is primarily configured to measure ion charge-state ratios within the plasma plume, offering valuable insights into thrust loss mechanisms, energy deposition, and sputter erosion of thruster and spacecraft surfaces. Several probe designs were described, along with guidance on proper implementation and operation. Methods for analyzing probe data to estimate the ion velocity distribution function (IVDF) and charge-state fractions were described. The paper also addressed corrections for ground test facility effects and included an uncertainty analysis. Finally, a comparative assessment of the ExB probe with other commonly used plume diagnostics was provided, highlighting their relative capabilities in characterizing ion velocity and energy distributions. The recommended practices outlined in this work aim to support experimentalists in the effective design and interpretation of ExB probe measurements, promoting consistency and accuracy across the field.

Acknowledgments

This work was partially supported by NASA through the Joint Advanced Propulsion Institute, a NASA Space Technology Research Institute, grant number 80NSSC21K1118. The authors thank Professor Kristina Lemmer for leading and organizing this series of recommended practices papers.

References

¹Dankanich, J. W., Walker, M., Swiatek, M. W., Yim, J. T., "Recommended practice for pressure measurement and calculation of effective pumping speed in electric propulsion testing," *Journal of Propulsion and Power*, Vol. 33, No. 3, pp. 668-680, 2017.

²Snyder, J. S., Baldwin, J., Frieman, J. D., Walker, M. L., Hicks, N. S., Polzin, K. A., Singleton, J. T., "Recommended practice for flow control and measurement in electric propulsion testing," *Journal of Propulsion and Power*, Vol. 33, No. 3, pp. 556-565, 2017.

³Polk, J. E., Pancotti, A., Haag, T., King, S., Walker, M., Blakely, J., Ziemer, J., "Recommended practice for thrust measurement in electric propulsion testing," *Journal of Propulsion and Power*, Vol. 33, No. 3, pp. 539-555, 2017.

- ⁴Brown, D. L., Walker, M. L., Szabo, J., Huang, W., Foster, J. E., "Recommended practice for use of Faraday probes in electric propulsion testing," *Journal of Propulsion and Power*, Vol. 33, No. 3, pp. 582-613, 2017.
- ⁵Lobbia, R. B., Beal, B. E., "Recommended practice for use of Langmuir probes in electric propulsion testing," *Journal of Propulsion and Power*, Vol. 33, No. 3, pp. 566-581, 2017.
- ⁶Sheehan, J., Raitses, Y., Hershkowitz, N., McDonald, M., "Recommended practice for use of emissive probes in electric propulsion testing," *Journal of Propulsion and Power*, Vol. 33, No. 3, pp. 614-637, 2017.
- ⁷Polzin, K. A., Hill, C. S., Turchi, P. J., Burton, R. L., Messer, S., Lovberg, R. H., Hallock, A. K., "Recommended practice for use of inductive magnetic field probes in electric propulsion testing," *Journal of Propulsion and Power*, Vol. 33, No. 3, pp. 659-667, 2017.
- ⁸Farnell, C. C., Farnell, S. C., Williams, J. D., "Recommended practice for use of electrostatic analyzers in electric propulsion testing," *Journal of Propulsion and Power*, Vol. 33, No. 3, pp. 638-658, 2017.
 - ⁹Goebel, D. M., Katz, I., Mikellides, I. G., *Fundamentals of Electric Propulsion*, Ch. 2, pp. 20-27, John Wiley & Sons, 2023. ¹⁰Goebel, D. M., Katz, I., Mikellides, I. G., *Fundamentals of Electric Propulsion*, Ch. 7, John Wiley & Sons, 2023.
- ¹¹Polk, J. E., "A critical review and meta-analysis of xenon-on-carbon sputter yield data," *Journal of Applied Physics*, Vol. 135, No. 4, 2024.
- ¹²Doerner, R. P., Whyte, D. G., Goebel, D. M., "Sputtering yield measurements during low energy xenon plasma bombardment," *Journal of Applied Physics*, Vol. 93, No. 9, pp. 5816-5823, 2003.
 - ¹³Wien, W., Verh. der Physik. Ges. Berlin, Vol. 16, pp. 165, 1897.
- ¹⁴Wien, W., "Untersuchungen über die electrische Entladung in verdünnten Gasen," *Annalen der Physik*, Vol. 301, No. 6, pp. 440-452, 1898.
- ¹⁵Plies, E., Marianowski, K., Ohnweiler, T., "The Wien filter: History, fundamentals and modern applications," *Nuclear Instruments and Methods in Physics Research Section A: Accelerators, Spectrometers, Detectors and Associated Equipment*, Vol. 645, No. 1, pp. 7-11, 2011.
- ¹⁶Tsuno, K., Ioanoviciu, D., "Chapter One Early History of Wien Filters," Advances in Imaging and Electron Physics, K. Tsuno and D. Ioanoviciu, eds., Elsevier, pp. 1-6, 2013.
- ¹⁷The Wien Filter, Advances in Imaging and Electron Physics, Vol. 176, T. Katsushige and D. Ioanoviciu, ed., Elsevier, 2013.
 ¹⁸Legler, W., "Ein modifiziertes Wiensches Filter als Elektronenmonochromator," *Zeitschrift für Physik*, Vol. 171, No. 2, pp. 424-435, 1963.
- ¹⁹Tsuno, K., "Monochromators in electron microscopy," *Nuclear Instruments and Methods in Physics Research Section A: Accelerators, Spectrometers, Detectors and Associated Equipment*, Vol. 645, No. 1, pp. 12-19, 2011.
- ²⁰Kienle, M., Plies, E., "An off-axis multi-channel analyzer for secondary electrons," *Nuclear Instruments and Methods in Physics Research Section A: Accelerators, Spectrometers, Detectors and Associated Equipment*, Vol. 519, No. 1-2, pp. 325-330, 2004.
- ²¹Tsuno, K., Ioanoviciu, D., Martinez, G., "Third-order aberration theory of Wien filters for monochromators and aberration correctors," *Journal of microscopy*, Vol. 217, No. 3, pp. 205-215, 2005.
- ²²Rose, H., "Aberration correction in electron microscopy," *International journal of materials research*, Vol. 97, No. 7, pp. 885-889, 2022.
- ²³Kang, Y., Hu, H., Zhao, J., "High order aberrations calculations of Wien filters using differential algebra methods," *Ultramicroscopy*, Vol. 210, pp. 112924, 2020.
- ²⁴Hawkes, P. W., Krivanek, O. L., "Aberration correctors, monochromators, spectrometers," Springer Handbook of Microscopy, Springer, pp. 625-675, 2019.
- ²⁵Bainbridge, K. T., "The Masses of Atoms and the Structure of Atomic Nuclei," *Journal of the Franklin Institute*, Vol. 215, No. 5, pp. 509-533, 1933.
 - ²⁶Seliger, R. L., "E×B Mass-Separator Design," Journal of Applied Physics, Vol. 43, No. 5, pp. 2352-2357, 1972.
- ²⁷Holmlid, L., "Mass dispersion and mass resolution in crossed homogeneous electric and magnetic fields: the Wien velocity filter as a mass spectrometer," *International Journal of Mass Spectrometry and Ion Physics*, Vol. 17, No. 4, pp. 403-421, 1975.
- ²⁸Quirós, E. L., "Some experimental facts that indicate the elimination of astigmatism in ion beams with separators using crossed electric and magnetic fields," *Journal of Applied Physics*, Vol. 52, No. 3, pp. 1152-1156, 1981.
- ²⁹Leal-Quiros, E., Prelas, M. A., "Focused high-intensity proton beam from a lithium source by using an E× B stigmatic selector," *Review of Scientific Instruments*, Vol. 61, No. 1, pp. 636-638, 1990.
- ³⁰Wrenger, B., Meiwes-Broer, K., "The application of a Wien filter to mass analysis of heavy clusters from a pulsed supersonic nozzle source," *Review of Scientific Instruments*, Vol. 68, No. 5, pp. 2027-2030, 1997.
- ³¹Ieshkin, A. E. e., Tolstoguzov, A. B., Korobeishchikov, N. G. e., Pelenovich, V., Chernysh, V. S. e., "Gas-dynamic sources of cluster ions for basic and applied research," *Uspekhi Fizicheskikh Nauk*, Vol. 192, No. 7, pp. 722-753, 2022.
- ³²Bischoff, L., Mazarov, P., Bruchhaus, L., Gierak, J., "Liquid metal alloy ion sources—An alternative for focussed ion beam technology," *Applied Physics Reviews*, Vol. 3, No. 2, 2016.
- ³³VAHRENKAMP, R., "Measurement of double charged ions in the beam of a 30-cm mercury bombardment thruster," AIAA 1973-1057, *AIAA 10th Electric Propulsion Conference*, Lake Tahoe, NV, Oct 31 Nov 2, 1973.
- ³⁴Vahrenkamp, R., "An experimental investigation of multiple ion processes in mercury bombardment thrusters," AIAA-75-397, *AIAA 11th Electric Propulsion Conference*, New Orleans, LA., Mar. 19-21, 1975.
- ³⁵Sovey, J., "Improved ion containment using a ring-cusp ion thruster," *Journal of Spacecraft and Rockets*, Vol. 21, No. 5, pp. 488-495, 1984.

- ³⁶Williams, G. J., Domonkos, M. T., Chavez, J. M., "Measurement of Doubly Charged Ions in Ion Thruster Plumes," IEPC-2001-310, 27th International Electric Propulsion Conference, Pasadena, CA, Oct. 14-19, 2001.
- ³⁷Pollard, J., Diamant, K., Crofton, M., Patterson, M., Soulas, G., "Spatially-resolved beam current and charge-state distributions for the next ion engine," AIAA-2010-6779, 46th AIAA/ASME/SAE/ASEE Joint Propulsion Conference & Exhibit, July 25-28, 2010.
- ³⁸Polk, J. E., Patterson, M. J., Brophy, J. R., Rawlin, V. K., Sovey, J. S., Myers, R. M., Blandino, J. J., Goodfellow, K. D., Garner, C. E., "A 1000 Hour Wear Test of the NASA NSTAR Ion Thruster," AIAA-96-2784, *32nd Joint Propulsion Conference and Exhibit*, Lake Buena Vista, FL, July 1-3, 1996.
- ³⁹Shastry, R., Herman, D., Soulas, G., Patterson, M., "NASA's Evolutionary Xenon Thruster (NEXT) Long-Duration Test as of 736 kg of Propellant Throughput," *48th AIAA/ASME/SAE/ASEE Joint Propulsion Conference & Exhibit*, pp. 4023,
- ⁴⁰Sengupta, A., Brophy, J., Anderson, J., Garner, C., Banks, B., Groh, K., "An overview of the results from the 30,000 hr life test of deep space 1 flight spare ion engine," AIAA-2004-3608, 40th AIAA/ASME/SAE/ASEE Joint Propulsion Conference and Exhibit, Fort Lauderdale, FL, July 11-14, 2004.
- ⁴¹Snyder, A., Kamhawi, H., Britton, M., Patterson, M., "Single-string integration test measurements of the next ion engine plume," AIAA-2004-3790, 40th AIAA/ASME/SAE/ASEE Joint Propulsion Conference and Exhibit, Fort Lauderadale, FL, July 11-14, 2004.
- ⁴²Kim, S.-W., "Experimental Investigations of Plasma Parameters and Species-Dependent Ion Energy Distributions in the Plasma Exhaust Plume of a Hall Thruster," Doctoral Thesis, Dept. of Aerospace Engineering, University of Michigan, Ann Arbor, MI, 1999.
- ⁴³Kim, S.-W., Gallimore, A. D., "Plume study of a 1.35-kW SPT-100 using an ExB probe," *Journal of Spacecraft and Rockets*, Vol. 39, No. 6, pp. 904-909, 2002.
- ⁴⁴Hofer, R., Gallimore, A., "Ion species fractions in the far-field plume of a high-specific impulse Hall thruster," AIAA-2003-5001, 39th AIAA/ASME/SAE/ASEE Joint Propulsion Conference and Exhibit, Huntsville, AL, July 20-23, 2003.
- ⁴⁵Hofer, R. R., Gallimore, A. D., "High-Specific Impulse Hall Thrusters, Part 2: Efficiency Analysis," *Journal of Propulsion and Power*, Vol. 22, No. 4, pp. 732-740, 2006.
- ⁴⁶Ekholm, J., Hargus, W., "ExB measurements of a 200 W xenon Hall thruster," AIAA-2005-4405, 41st AIAA/ASME/SAE/ASEE Joint Propulsion Conference & Exhibit, Tucson, AZ, July 10-13, 2005.
- ⁴⁷Reid, B., Shastry, R., Gallimore, A., Hofer, R., "Angularly-Resolved ExB Probe Spectra in the Plume of a 6-kW Hall Thruster," AIAA-2008-5287, 44th AIAA/ASME/SAE/ASEE Joint Propulsion Conference & Exhibit, Hartford, CT, July 21-23, 2008.
- ⁴⁸Sullivan, R. M., Yost, A., Johnson, L. K., "Near-field angular distributions of high velocity ions for low-power hall thrusters," *2009 IEEE Aerospace conference*, Big Sky, MT, Mar. 7-14, 2009.
- ⁴⁹Diamant, K., Spektor, R., Beiting, E., Young, J., Curtiss, T., "The effects of background pressure on Hall thruster operation," 48th AIAA/ASME/SAE/ASEE Joint Propulsion Conference & Exhibit, pp. 3735,
- ⁵⁰Diamant, K. D., Curtiss, T. J., Spektor, R., Beiting, E. J., Hruby, V., Pote, B., Kolencik, J., Paintal, S., "Performance and plume characterization of the BHT-1500 Hall thruster," IEPC-2015-69, *Joint Conference of 30th International Symposium on Space Technology and Science, 34th International Electric Propulsion Conference, and 6th Nano-satellite Symposium*, Hyogo-Kobe, Japan, July 4-10, 2015.
- ⁵¹Diamant, K. D., Lee, T., Liang, R., Noland, J., Vial, V., Cornu, N., "Performance and plume characterization of the PPS 1350-G Hall thruster," AIAA-2016-4543, *52nd AIAA/SAE/ASEE Joint Propulsion Conference*, Salt Lake City, UT, July 25-27, 2016.
- ⁵²Gurciullo, A., Fabris, A. L., Cappelli, M. A., "Ion plume investigation of a Hall effect thruster operating with Xe/N2 and Xe/air mixtures," *Journal of Physics D: Applied Physics*, Vol. 52, No. 46, pp. 464003, 2019.
- ⁵³Watanabe, H., Cho, S., Kubota, K., "Performance and plume characteristics of an 85 W class Hall thruster," *Acta Astronautica*, Vol. 166, pp. 227-237, 2020.
- ⁵⁴Hall, S. J., Jorns, B. A., Gallimore, A. D., Kamhawi, H., Huang, W., "Plasma Plume Characterization of a 100 kW Nested Hall Thruster," *Journal of Propulsion and Power*, Vol. 38, No. 1, pp. 97-110, 2022.
- ⁵⁵Peterson, P., Jacobson, D., Manzella, D., John, J., "The Performance and Wear Characterization of a High-Power High-Isp NASA Hall Thruster," AIAA-2005-4243, 41st AIAA/ASME/SAE/ASEE Joint Propulsion Conference & Exhibit, Tucson, AZ, July 10-13, 2005.
- ⁵⁶Frieman, J. D., Kamhawi, H., Peterson, P. Y., Herman, D. A., Gilland, J. H., Hofer, R. R., "Completion of the long duration wear test of the NASA HERMeS Hall thruster," AIAA-2019-3895, *AIAA Propulsion and Energy 2019 Forum*, Indianapolis, IN, Aug 19-22, 2019.
- ⁵⁷Yamauchi, T., Rovey, J., "Analysis of the ion collection model in the ExB probe," *Journal of Electric Propulsion*, Vol. 3, No. 1, pp. 10, 2024.
- ⁵⁸Huang, W., Shastry, R., "Analysis of Wien filter spectra from Hall thruster plumes," *Review of Scientific Instruments*, Vol. 86, No. 7, 2015.
- ⁵⁹Lim, Y., Kim, H., Choe, W., Lee, S. H., Seon, J., Lee, H. J., "Observation of a high-energy tail in ion energy distribution in the cylindrical Hall thruster plasma," *Physics of Plasmas*, Vol. 21, No. 10, 2014.
- ⁶⁰Beattie, J. R., "Extended Performance Technology Study: 30-cm Thruster," Final Report, NASA CR-168259, Hughes Research Laboratories, June 1983.
- ⁶¹Yamauchi, T., Tompkins, J., Rovey, J., "Development of the dual-collector ExB probe," AIAA-2025-1669, *AIAA SCITECH 2025 Forum*, Orlando, FL, Jan. 2025.

- ⁶²Sroubek, Z., Lorincik, J., "Kinetic electron emission from metal surfaces induced by impact of slow ions," *Surface science*, Vol. 625, pp. 7-9, 2014.
- ⁶³Jousten, K., Boineau, F., Bundaleski, N., Illgen, C., Setina, J., Teodoro, O. M., Vicar, M., Wüest, M., "A review on hot cathode ionisation gauges with focus on a suitable design for measurement accuracy and stability," *Vacuum*, Vol. 179, pp. 109545, 2020.
- ⁶⁴Huerta, C. E., Wirz, R. E., "Ion-induced electron emission reduction via complex surface trapping," *AIP advances*, Vol. 9, No. 12, 2019.
- ⁶⁵Hagstrum, H. D., "Auger ejection of electrons from tungsten by noble gas ions," *Physical Review*, Vol. 96, No. 2, pp. 325, 1954.
- ⁶⁶Hagstrum, H. D., "Auger ejection of electrons from molybdenum by noble gas ions," *Physical Review*, Vol. 104, No. 3, pp. 672, 1956.
- ⁶⁷Hagstrum, H. D., "Auger ejection of electrons from tungsten by noble gas ions," *Physical Review*, Vol. 104, No. 2, pp. 317, 1956
- ⁶⁸Farnell, C. C., Brown, D. L., Willis, G., Branam, R., Williams, J. D., "Remote diagnostic measurements of Hall thruster plumes," IEPC-2009-031, 31st International Electric Propulsion Conference, Sept 20-24, 2009.
- ⁶⁹Brown, D. L., Larson, C. W., Beal, B. E., Gallimore, A. D., "Methodology and historical perspective of a Hall thruster efficiency analysis," *Journal of Propulsion and Power*, Vol. 25, No. 6, pp. 1163-1177, 2009.
- ⁷⁰Maldonado, C., Ketsdever, A., "Source Characterization for a Combined Effects Space Simulation Facility," AIAA-2013-0808, 51st AIAA Aerospace Sciences Meeting including the New Horizons Forum and Aerospace Exposition, Grapevine, TX, Jan 7-10, 2013.
- ⁷¹Young, J. A., Matlock, T., Nakles, M., Crofton, M. W., Patterson, M. J., Arthur, N. A., John, J., "Far Field Plume Distribution and Divergence for NEXT: DART Mission," AIAA-2019-1243, *AIAA Scitech 2019 Forum*, San Diego, CA, Jan. 7-11, 2019.
- ⁷²Huang, W., Kamhawi, H., "The Side Plume of Magnetically Shielded Hall Thrusters," IEPC-2022-402, *37th International Electric Propulsion Conference*, Cambridge, MA, July 19-23, 2022.
- ⁷³Yim, J. T., Huang, W., Allen, M. G., "Extraction of thruster plume ion population trends from retarding potential analyzer data," IEPC-2024-116, 38th International Electric Propulsion Conference, Toulouse, France, June 23-28, 2024.
- ⁷⁴Huang, W., Kamhawi, H., Haag, T., Ortega, A. L., Mikellides, I. G., "Facility effect characterization test of NASA's HERMeS Hall thruster," AIAA-2016-4828, *52nd AIAA/SAE/ASEE Joint Propulsion Conference*, Salt Lake City, UT, July 25-27, 2016.
- ⁷⁵Coey, J. M. D., "Perspective and Prospects for Rare Earth Permanent Magnets," *Engineering*, Vol. 6, No. 2, pp. 119-131, 2020.
- ⁷⁶Xia, W., He, Y., Huang, H., Wang, H., Shi, X., Zhang, T., Liu, J., Stamenov, P., Chen, L., Coey, J. M. D., Jiang, C., "Initial Irreversible Losses and Enhanced High-Temperature Performance of Rare-Earth Permanent Magnets," *Advanced Functional Materials*, Vol. 29, No. 24, pp. 1900690, 2019.
- ⁷⁷Lee, S. H., Kim, J., Lee, J. H., Choe, W., "Modified Phillips–Tikhonov regularization for plasma tomography," *Current Applied Physics*, Vol. 10, No. 3, pp. 893-899, 2010.
- ⁷⁸Buccini, A., Donatelli, M., Reichel, L., "Iterated Tikhonov regularization with a general penalty term," *Numerical Linear Algebra with Applications*, Vol. 24, No. 4, pp. e2089, 2017.
- ⁷⁹Iwama, N., Yoshida, H., Takimoto, H., Shen, Y., Takamura, S., Tsukishima, T., "Phillips–Tikhonov regularization of plasma image reconstruction with the generalized cross validation," *Applied Physics Letters*, Vol. 54, No. 6, pp. 502-504, 1989.
- ⁸⁰Park, Y., Reichel, L., Rodriguez, G., Yu, X., "Parameter determination for Tikhonov regularization problems in general form," *Journal of Computational and Applied Mathematics*, Vol. 343, pp. 12-25, 2018.
- ⁸¹Shastry, R., Hofer, R. R., Reid, B. M., Gallimore, A. D., "Method for analyzing E×B probe spectra from Hall thruster plumes," *Review of Scientific Instruments*, Vol. 80, No. 6, 2009.
- ⁸²Thomas, R. E., Gonzalez, M. C., Raju, R. S., Bontempo, J. J., Goodfellow, K. D., Aubuchon, C. A., Patterson, M. J., "Development Status and Performance Metrics of the Advanced NEXT Ion Propulsion System," *39th International Electric Propulsion Conference*, London, United Kingdom, Sept 14-19, 2025.
- ⁸³Diamant, K. D., Pollard, J. E., Crofton, M. W., Patterson, M. J., Soulas, G. C., "Thrust Stand Characterization of the NASA Evolutionary Xenon Thruster (NEXT)," AIAA-2010-6701, 46th Joint Propulsion Conference and Exhibit, Nashville, TN, July 25-28, 2010.
- ⁸⁴Huang, W., Shastry, R., Soulas, G., Kamhawi, H., "Farfield Plume Measurement and Analysis on the NASA-300M and NASA-300MS," IEPC-2013-057, *33rd International Electric Propulsion Conference*, George Washington University, Oct 6-10, 2013.
- ⁸⁵Beal, B. E., "Clustering of Hall Effect Thrusters for High-Power Electric Propulsion Applications," PhD Thesis, Dept. of Aerospace Engineering, University of Michigan, Ann Arbor, MI, 2004.
- ⁸⁶Linnell, J. A., "An Evaluation of Krypton Propellant in Hall Thrusters," PhD Thesis, Dept. of Aerospace Engineering, University of Michigan Ann Arbor, MI, 2007.
 - ⁸⁷Rosenthal, J. S., A First Look At Rigorous Probability Theory, 2nd Ed., WSPC, Singapore, 2006.
- ⁸⁸Hurley, W. J., Jorns, B. A., "Mass utilization scaling with propellant type on a magnetically shielded Hall thruster," *Plasma Sources Science and Technology*, Vol. 34, No. 5, pp. 055010, 2025.
- ⁸⁹Thompson, S. J., Farnell, S. C., Farnell, C. C., Farnell, C. C., Andreano, T. M., Williams, J. D., "Combined electrostatic analyzer—Wien filter probe for characterization of species distributions in Hall thrusters," *Journal of Applied Physics*, Vol. 130, No. 23, 2021.